

# Neuromorphic Skin Based on Emerging Artificial Synapses

Yeongjun Lee, Jin Young Oh, and Tae-Woo Lee\*

**Neuromorphic skin is an emerging electronic skin that demonstrates sensory, memory, learning, and motor responses in a neuromorphic way by using advanced artificial synaptic devices that emulate the biological nervous system and its neural plasticity. Many types of artificial synapses that emulate brain-inspired computing have been developed and are being integrated in electronic skin to demonstrate artificial sensory and motor nervous systems. The neuromorphic skin, which operates using voltage spikes thereof, precisely mimics the energy-efficient information processing of biological nervous system in the brain and body and enables the implementation of power- and time-efficient cognitive sensors and computing, biomimetic robotics and electronics, and biocompatible neuroprosthetics. Here, biological synapses and emerging artificial synapses are introduced, and recent research is reviewed on neuromorphic skins that use artificial synapses for sensing, memory, learning, and motor systems. Finally, the outlook and challenges to be addressed are provided for future advanced neuromorphic skin in which all neuromorphic parts are integrated with brain-inspired computing and bioinspired robotics.**

## 1. Introduction

Neuromorphic engineering is an emerging technology to develop biomimetic electronics and robotics by mimicking

Y. Lee, T.-W. Lee  
Department of Materials Science and Engineering  
Seoul National University  
Seoul 08826, Republic of Korea  
E-mail: twlees@snu.ac.kr

Y. Lee  
Department of Chemical Engineering  
Stanford University  
Stanford, CA 94305, USA

J. Y. Oh  
Department of Chemical Engineering (Integrated Engineering Program)  
Kyung Hee University  
Yongin 17104, Republic of Korea

T.-W. Lee  
Institute of Engineering Research  
Research Institute of Advanced Materials  
Soft Foundry  
Seoul National University  
Seoul 08826, Republic of Korea

T.-W. Lee  
School of Chemical and Biological Engineering  
Seoul National University  
Seoul 08826, Republic of Korea

 The ORCID identification number(s) for the author(s) of this article can be found under <https://doi.org/10.1002/admt.202200193>.

DOI: 10.1002/admt.202200193

biological neural systems such as brains and nerves.<sup>[1,2]</sup> Although the complementary metal-oxide-semiconductor (CMOS) technology has been remarkably developed and enabled digital revolution during the last decades, the current computing and electronic systems are expected to encounter limitations in the upcoming era of artificial intelligence (AI).<sup>[3]</sup> Moore's law may be no longer applicable,<sup>[4]</sup> so further downscaling and integration, and decrease in the energy consumption of processors is becoming difficult; consequently, supercomputers for AI to process big data require huge numbers of processing chips. Graphic processing units (GPUs) have been used as core elements for efficient parallel implementation of vector-matrix multiplication (VMM) in deep learning,<sup>[5]</sup> but in the classic von Neumann structure, processing units are separated from memory cells, so data must be shuttled through buses; this process

constrains speed and reduction of energy usage. This is the "von Neumann bottleneck"; it restricts the efficiencies of time and energy in current digital computing system.<sup>[6]</sup> Moreover, numerous central processing units (CPUs) and GPUs make supercomputers bulky and heavy.

A brain has slow computational speed and low calculation accuracy compared to the digital supercomputer, but efficiently performs comprehensive functions such as learning, recognition, judge, memory, and controlling homeostasis and somatic/autonomic nervous systems, while consuming little power ( $\approx 20$  W).<sup>[7]</sup> Neurons and synapses are the fundamental components of biological nervous system including the central nervous system (CNS; i.e., the brain and spinal cord), and peripheral nervous system (PNS; i.e., sensory and motor nerves). A human brain is composed of  $\approx 10^{12}$  neurons are interconnected by  $\approx 10^{15}$  synapses. The neurons are entangled with high compactness in three-dimensional and massively-parallel networks.<sup>[8]</sup> The brain implements processing and memory together with extremely low energy consumption of  $\approx 10$  fJ per synaptic event.<sup>[9]</sup> Moreover, the brain use asynchronous event-responsive operation that spends power only with input events, whereas most computing systems that use CPUs with von Neumann architecture operate with a synchronous clock that consumes power periodically, regardless of whether the unit is active.<sup>[10]</sup>

A brain communicates with sensory and motor organs in the body by transmitting neural signals through neurons and synapses of afferent and efferent nerves in the PNS. With sensory input, an afferent nerve transfers neural signals from sensory cells to CNS, then the brain makes decisions, which

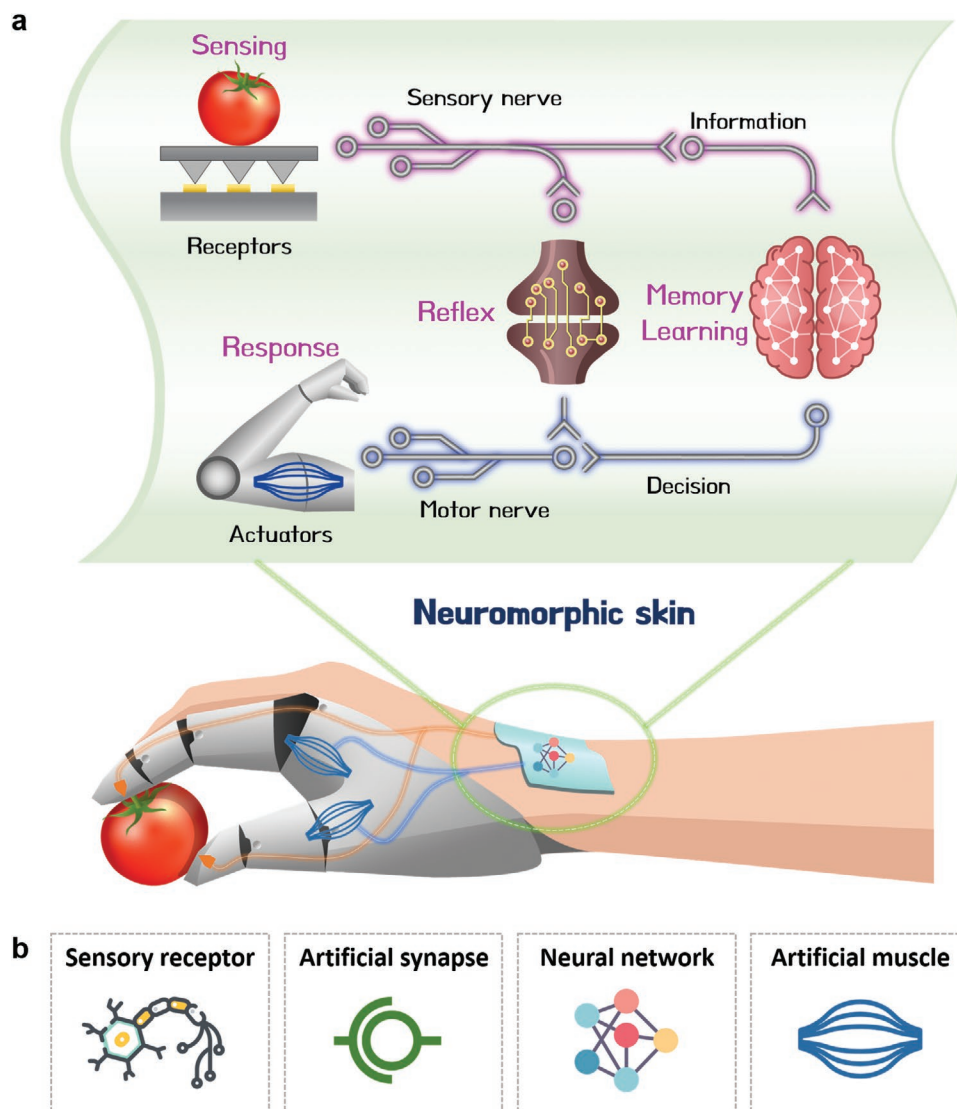


**Figure 1.** Schematics of a) neuromorphic skin, an electronic skin that mimics the biological nervous system and neural plasticity to demonstrate sensory, memory and learning, and motor responses in a neuromorphic way, and b) main components of neuromorphic skin.

are transmitted along efferent nerves to muscle cells, which actuate motor output. This process that connects real-time data processing with cognition of and reaction to the external environment has become one of important tasks in AI research. For example, autonomous vehicles collect huge volume of images around the road, and must analyze it to identify and perform optimal decisions according to the surrounding situation.<sup>[11–13]</sup> The movement of an autonomous vehicle is a kind of output behavior to the external environment. To monitor surrounding, millions of pixels are required,<sup>[14]</sup> they collect a huge amount of data, which must be processed rapidly and accurately in real time.<sup>[15]</sup> The energy efficiency and data processing speed can be increased by using neuromorphic cognitive sensors and computing systems, which implement the cognition, data processing, and decision making in a neuromorphic manner.<sup>[16]</sup> Moreover, neuromorphic sensors that have the intelligence to classify incoming data and to

autonomously respond to complex interactions, would reduce the amount of data transmission to central computing processors or cloud servers.<sup>[17,18]</sup> This reduction will increase computation speed and power efficiencies, and alleviate privacy concerns.<sup>[19,20]</sup>

Neuromorphic devices can also recognize, learn and respond to various stimuli such as touch, pressure, strain, chemicals, temperature, sound, and multimodal stimuli.<sup>[12,13,21–27]</sup> Moreover, flexible and stretchable devices would be essential for future computing and robotic devices such as wearable user interfaces, augmented reality, mobile health monitoring, human-like robots, and electronic prosthesis.<sup>[28,29]</sup> Neuromorphic engineering would provide neuromorphic electronic skin (neuromorphic skin) that can offer soft, biomimetic and low-power human-integrated neuromorphic electronic and robotic applications (**Figure 1**). Thus, neuromorphic skin that mimics biological neural signal transmission can be a next-generation

hardware system, by connecting biological and artificial neural signals.

In this report, we review recent progress in development and applications of neuromorphic skin devices that use emerging artificial synapses. We first introduce the structure and working mechanism of biological synapses and artificial synapses. Next, we review examples of neuromorphic skin devices that use artificial synapses for sensing, especially with artificial photoreceptors, mechanoreceptors and nociceptors which are more widely emulated receptors than other sensory receptors. Then we present examples of neuromorphic skin devices with artificial synapses that use voltage spikes to achieve memory and learning. We also depict examples of neuromorphic skin devices that use artificial synapses for motor systems for use in future biomimetic robotics and biohybrid applications. Last, we suggest the outlook and challenges for the future advanced neuromorphic skin.

## 2. Biological and Artificial Synapses

### 2.1. Biological Synapses

In biology, chemical synapses transfer chemical neurotransmitters between pre- and post-neurons through a very narrow gap (20-40 nm) called a synaptic cleft.<sup>[30]</sup> The pre-neuron located before the synapse, action potentials are transmitted along the axon and reach its terminal, then  $\text{Ca}^{2+}$  ions move inside the membrane through ion channels.<sup>[31]</sup> Vesicles that contain neurotransmitters then move towards dendrites, and release the neurotransmitters at dendrite membranes. The released neurotransmitters (e.g., acetylcholine) are captured by receptors on postsynaptic membranes, then ion channels in the postsynaptic membranes are opened.<sup>[32]</sup> Ion exchange through the ion channels induces polarization of postsynaptic membrane potentials, which are delivered to a soma, which integrates potentials received from numerous dendrites.<sup>[33]</sup> When the integrated potential results exceed a threshold, the postsynaptic neuron generates action potentials which propagate along the axon to synapses that connect the postsynaptic neuron to the next neurons.

According to the action potential firing rate, synaptic plasticity is changed.<sup>[34]</sup> When action potential firing is repetitive and relatively frequent, the strength of synaptic connection of two neurons (synaptic strength) is increased by an increase in the number of receptors that bind neurotransmitters, and also by formation of new synaptic junctions. These changes strengthen synaptic connections (i.e. synaptic weight); these changes are related to learning and training.<sup>[35]</sup> In contrast, when action potential firing is non-repetitive and infrequent, synaptic strength is weakened by degeneration of receptors and synapses;<sup>[36]</sup> these changes decrease synaptic strength, and are causes of forgetting and detraining.<sup>[37]</sup> The action potential firing rate and temporal dependencies of synaptic weight are main mechanisms by which artificial synapses emulate update of synaptic weight in a spiking neural network (SNN) which is an emerging neural network (NN) that mimics working behaviors of biological spiking neurons and synapses.<sup>[38]</sup>

Neurons and synapses are also connected by unidirectional serial connections in the PNS. In a sensory system, action potentials are fired from sensory receptors of sensory neurons by external input stimulation.<sup>[39,40]</sup> The action potentials are then transmitted to the connected neurons in the body through synapses. Depending on the amplitude and repetition of stimuli, the action potential firing frequency of a spiking sensory neuron changes, so sensory information is transferred to the brain. In the somatic motor system, the brain sends motor signals to the muscle fibers through the upper and lower motor neurons and makes muscles contract.<sup>[41]</sup> Most research on electronic skin devices has focused on developing highly-responsive sensors and actuators, which are driven by digital circuits.<sup>[42–46]</sup> Recently, several studies of the development of artificial sensory and motor nerves have emulated biological sensory and motor nerves that transmit information by using spike signals.<sup>[47–49]</sup> These neuromorphic skin devices would have applications as biomedical devices, neural prostheses, and humanoid robots.

### 2.2. Artificial Synapses

Software algorithms for machine learning, e.g., deep neural networks (DNNs) that have multiple hidden layers, are powerful to implement AI, as a result of development of backpropagation algorithm and high performance GPUs.<sup>[3]</sup> However, because of the von Neumann bottleneck, implementation of numerous VMMs is slow and uses large power.<sup>[6]</sup> A memory (e.g., 2-terminal and 3-terminal non-volatile memories) crossbar network may overcome the CMOS technology's limitations by efficiently using Ohm's law and Kirchhoff's current law. With advantages of simple structure, non-volatility with long retention, low power consumption, fast switching speed, and high endurance, emerging memory devices that will be introduced in the following chapters and their conductance in the crossbar network have been used as synapses and synaptic weight respectively in artificial neural networks (ANNs).<sup>[50,51]</sup> To update synaptic weight efficiently and accurately, gradual state switching with analog-like continuous conductance states that are linear and symmetric is necessary.<sup>[52]</sup> Therefore, numerous artificial synapse devices with various working mechanisms have been developed to emulate the characteristics of biological synapses to achieve brain-inspired computing and biomimetic robotic applications.

#### 2.2.1. Charge-Based Artificial Synapses

Flash memory is a mature silicon technology that is non-volatile data storage that uses floating-gated or charge-trap flash (CTF) transistors.<sup>[53]</sup> The floating-gated transistor has two gates; one is a control gate which is a common gate of a transistor and the other is a floating gate that is surrounded by insulating layers (tunneling and gate insulator layers) and located between the control gate and semiconductor channel (**Figure 2a**). In the CTF, an insulating charge trapping layer with numerous trap sites replaces the floating gate (**Figure 2b**). These memory transistors exploit trapping of charge carriers in a floating gate or a charge trapping layer by

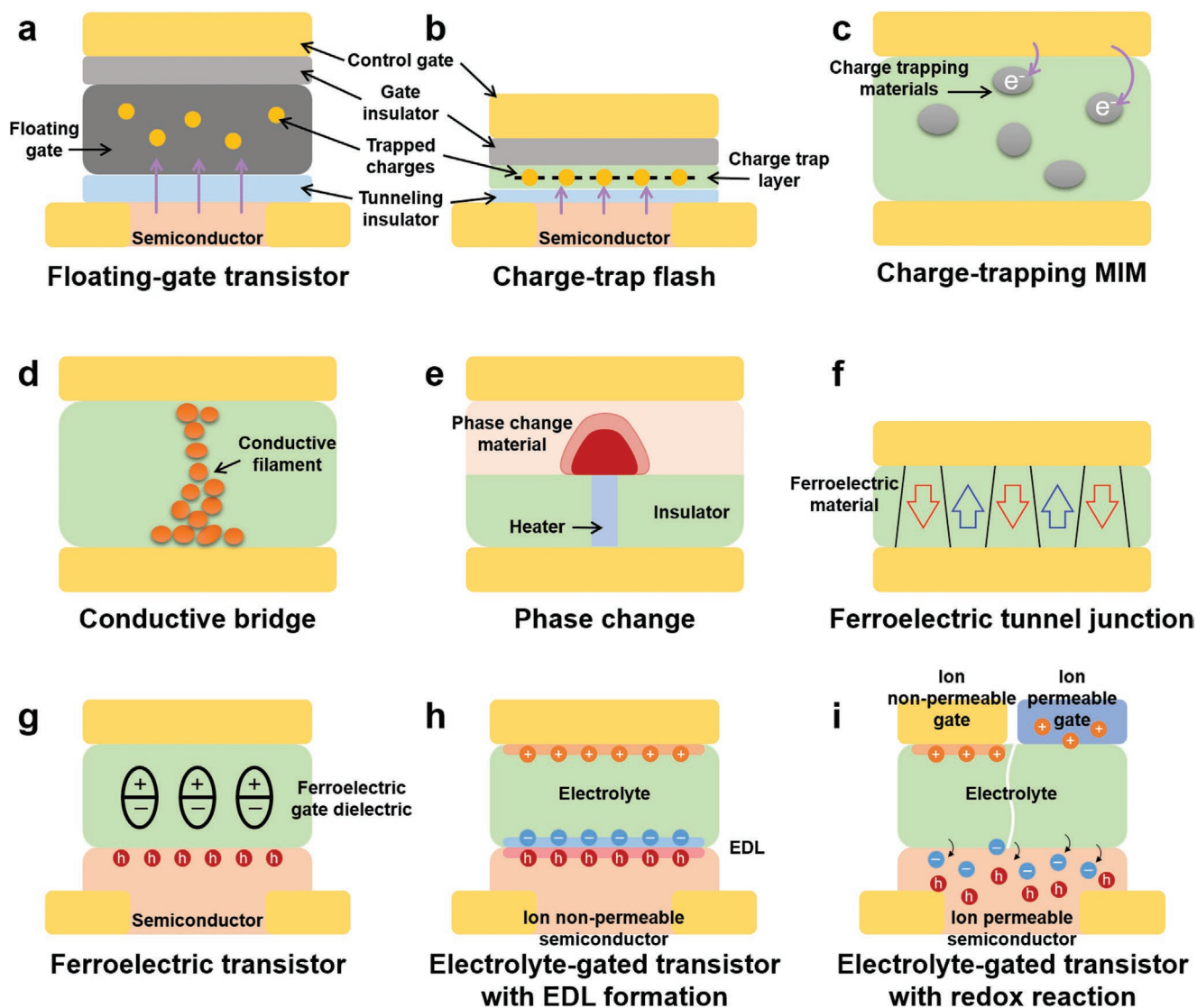


**Figure 2.** Schematics of artificial synapses with device geometries of a) floating-gate transistor, b) charge-trap flash, c) charge-trapping MIM, d) conductive bridge, e) phase change, f) ferroelectric tunnel junction, g) ferroelectric transistor, and electrolyte-gated transistors with h) EDL formation and i) redox reaction.

a control gate. Once charges are trapped in the charge storage layer, the electric field from the control gate is affected by the trapped charges, so the threshold voltage  $V_{th}$  undergoes a shift  $\Delta V_{th}$ . An opposite electric field from the control gate releases the trapped charges in the charge storage layer to the semiconductor channel; this process returns  $V_{th}$  to the initial value. The charge trapping also can be controlled by voltage spikes and demonstrate synaptic plasticity.<sup>[54–56]</sup> Charge-trapping transistors that do not use silicon have been demonstrated for next-generation neuromorphic engineering.<sup>[57–66]</sup> For example, charge-trapping transistors with interfacial traps between semiconductor and dielectric layers or conductive nanomaterials (e.g., Au nanoparticles or  $C_{60}$ ) dispersed in the semiconductor layer have synaptic plasticity.<sup>[57–66]</sup>

Metal-insulator-metal (MIM)-structured two-terminal memory and synapse devices with randomly-dispersed charge trapping nanomaterials in the middle insulating layer

have memory characteristics that exploit charge trapping (Figure 2c).<sup>[67–70]</sup> The electron-injection mechanism follows thermionic emission-limited current, Ohmic, trap-limited space charge limited current (trap-limited SCLC), trapped-charge-limited current, or trap-free space-charge-limited current (trap-free SCLC) conduction. At low voltage with Ohmic conduction, the number of electrons injected from the electrode is less than the number of thermally-activated charges in the insulating layer. At high voltage, the injected electrons outnumber the thermal charges and start to fill traps; the current follows the trap-limited SCLC conduction. When traps are fully charged by numerous injected charges, the current follows trap-free SCLC conduction. The reverse voltage bias releases trapped charges to the insulating medium and the electrode. Also, these memory devices can spontaneously and slowly release trapped charges without the reverse voltage bias; this phenomenon is an impediment to achieving long-term memory retention.

### 2.2.2. Resistance-Based Artificial Synapses

**Conductive Bridge-Type Resistive Synapse:** A two-terminal resistive memory that exploits electrochemical metallization operates by formation of conductive metallic filaments (“set” process) that yield an LRS, and rupture of the filaments (“reset” process) to return to a high-resistance state (HRS) (Figure 2d).<sup>[71–76]</sup> Applied voltage oxidizes the active metal electrode, then oxidized metal ions are drifted toward the opposite electrode by electric field. Metal ions are reduced by electrons at the opposite electrode to metal nanoparticle clusters that form metallic filaments; this ‘set’ process induces abrupt increase of current with a low-resistance state (LRS). During ‘reset’ process with Joule heating or electrochemical oxidation of the filaments, the metallic bridges are disrupted and the conductance state returned to HRS. The memory retention of the device is limited by spontaneous rupture of the filament due to minimization of interfacial energy or the Gibbs-Thomson effect. Oxygen-vacancy drift is another mechanism, it is used in oxide resistive memory devices that operate by formation of conductive filaments.<sup>[72–76]</sup> The construction of conductive filaments changes conductance abruptly, so nonlinear and asymmetric synaptic weight update in the resistive switching synapses can occur. Linear and symmetric conductance modulation between LTP and LTD has been precisely demonstrated by using voltage pulses that have identical or ramping amplitudes.<sup>[77–79]</sup>

**Phase Change Synapse:** Phase-change memory devices have top and bottom electrodes that are separated by a phase-change material that changes reversibly between LRS crystalline phase and HRS amorphous phase (Figure 2e).<sup>[80–82]</sup> When subjected to a short, high-amplitude electric pulse to induce rapid Joule heating to high temperature above the crystalline temperature, followed by rapid quenching, a localized region of the LRS crystalline phase changes to amorphous phase; this abrupt ‘reset’ process results in HRS. Then, when subjected to a relatively long and ramping amplitude electric pulse to induce slow Joule heating with temperature above the crystalline temperature, followed by slow cooling, the amorphous region recrystallizes to the LRS (‘set’ process). The incremental set process and abrupt reset process can cause nonlinear and asymmetric synaptic weight modulation. Therefore, linear and multistate conductance modulation has been demonstrated with electrode dimension modulation, integration of two phase-change memory devices, and an appropriate pulse scheme.<sup>[83–85]</sup>

**Ferroelectric Tunnel Junction Synapse:** Non-volatile memory with ferroelectric tunnel junctions modulates polarization of a thin ferroelectric layer sandwiched between two electrodes with an applied electric field (Figure 2f).<sup>[86–89]</sup> The tunneling electroresistance, which is the height of the barrier to electron tunneling through the tunnel junction is controlled by the direction of ferroelectric polarization and the related electrostatic charge-screening effect. The gradually-controlled polarization of the ferroelectric layer is retained when the electric field is turned off; this phenomenon enables analog switching of non-volatile conductance states. The thickness of the ferroelectric layer is a few nanometers and the tunneling current is typically small, so the switch between conductance states requires little energy. Also, the large tunneling electroresistance increases tolerance to reading errors, and reduces energy consumption. The

ferroelectric resistance is controlled by nucleation and propagation of polarized domains with consecutive voltage pulses of varied amplitude.<sup>[90,91]</sup> Asymmetry and abrupt switching behaviors of resistance can occur during the voltage sweep cycle. Therefore, linear and symmetric conductance states on logarithmic or linear scales have been precisely modulated by using voltage pulses that have identical or ramping amplitudes.<sup>[90–93]</sup>

**Ferroelectric Synaptic Transistor:** Ferroelectric polarization can also control the channel conductance of transistors that have ferroelectric gate dielectrics (Figure 2g).<sup>[94–101]</sup> Hafnium oxide (HfO<sub>2</sub>), an inorganic oxide that has a high-dielectric-constant and has ferroelectric characteristics when mixed with zirconium oxide (ZrO<sub>2</sub>), has been extensively studied for use in CMOS technology.<sup>[94–98]</sup> Also, poly(vinylidene fluoride)-trifluoroethylene (PVDF-TrFE) is an organic ferroelectric copolymer; it has been widely applied as a gate insulator in ferroelectric transistors and memory devices.<sup>[99–101]</sup> During gate-voltage sweeps, the drain-current/gate-voltage characteristics of ferroelectric transistors has hysteresis caused by electric-field-dependent dipole alignment, which induces charge carriers in the channel region. The ferroelectric transistors have a high on/off current ratio, fast switching speed, stable memory retention and endurance during voltage sweep cycles.<sup>[102]</sup> For analog multi-state synaptic memory, a voltage pulse of ramping amplitude induced a more linear and symmetric conductance switching than a pulse that had identical amplitude.<sup>[97–99]</sup>

**Electrolyte-Gated Synaptic Transistors:** Electrolyte-gated transistors are resistive memory devices that can have either volatile or non-volatile analog-like conductance switching.<sup>[103–105]</sup> Voltage-dependent migration of ions in the electrolyte modulates the channel conductance of transistor by forming an electric double layer (EDL) or undergoing an electrochemical redox reaction.<sup>[106–108]</sup> In the electrolyte-gated transistors with channel materials that do not have ion permeation, intercalation, or penetration, ion migration forms an EDL near the surface of semiconductor layers upon which the voltage is applied, and induces temporary increase in channel conductance (Figure 2h).<sup>[109–112]</sup> When the voltage is removed, the current decay is fast but not abrupt, because spontaneous relaxation of migrated ions takes a short time. This is a short-term memory effect, and analogous to short-term potentiation of the nervous system. In contrast, electrolyte-gated transistors with channel materials that have ion permeation,<sup>[113–115]</sup> intercalation,<sup>[116–118]</sup> penetration,<sup>[119–121]</sup> or surface hydrogenation<sup>[122]</sup> undergo electrochemical redox reactions by which ions migrate into and interact with the channel materials when voltage is applied (Figure 2i). When voltage is off, relatively slow spontaneous reverse redox reaction occurs; so such doping effects are retained for a long time and the current decays slowly. Moreover, the device that has both an ion permeable semiconductor channel and a gate electrode (e.g., battery-like synapses), demonstrate non-volatile and multistate (>500) potentiation and depression.<sup>[123]</sup> This is a long-term memory effect, and is analogous to long-term potentiation in the nervous system.

**Organic Memristive Synapse with Electrochemical Redox Response:** When unshared pairs of electrons in iron of ferrocene,<sup>[124,125]</sup> nitrogen of triphenylamine,<sup>[126]</sup> and iron of terpyridyl-iron polymer<sup>[127]</sup> are easily removed by external electric field, the organic material is oxidized, form a cationic

conducting pathway in the backbone, and add an impurity energy level to the bandgap.<sup>[127]</sup> Therefore, the conductivity of the organic material increases abruptly. The oxidized state is maintained stably in the air<sup>[124]</sup> or is neutralized by an anion (e.g.  $\text{ClO}_4^-$  in ethyl viologen doperchlorate  $[\text{EV}(\text{ClO}_4)_2]$ ) reduced from an electrolyte that is stacked together to maintain an oxidized state stably for a long time.<sup>[126,128]</sup> The organic material is reduced by the reverse electric field, the anion moves back to the electrolyte (e.g., 4,4'-bipyridine salt), and the electrolyte is reoxidized.<sup>[129]</sup> Accordingly, the conductivity of the organic material decreases. In addition, redox reactions of organic materials and electrolytes can be continuously controlled, thereby continuous modulation of conductivity is possible with voltage pulses that have identical amplitude.<sup>[129]</sup>

### 3. Neuromorphic Skin That Uses Artificial Synapses for Sensing

Numerous electronic skin sensory receptors that have greater sensitivity than biological sensory organs have been reported,<sup>[130–132]</sup> but relays in a sensory nervous system have not been considered. Also, computing systems that analyze big data received from sensors (e.g., a high-resolution image sensor) have been developed using NN systems that are emulated in software.<sup>[19,133]</sup> To improve data-processing efficiencies and reduce energy cost, the development of neuromorphic sensory and computing hardware must be advance, and this is one of the ultimate goals of neuromorphic engineering. The research paradigm has been changed from ‘sensor’ to ‘sense’, so neuromorphic cognitive sensors that use artificial sensory synapses that operate using spike signals have been reported.<sup>[8,24,47,49,134,135]</sup> These synapses will enable development of cognitive computing systems that use neuromorphic hardware, and of wearable neuromorphic robotic/bioengineering systems.

#### 3.1. Photoreceptors

The retinas of vertebrate eyes include rod cells ( $\approx 90$  million in a human eye) and cone cells ( $\approx 6$  million in a human eye). The rod cells are responsible for night vision in dim light, whereas the three types of cone cells that have different sensitivities to wavelengths of visible light are responsible for color vision in bright light (Figure 3a). These photoreceptor cells are connected to other neurons such as bipolar cells and ganglion cells by synaptic junctions with neurotransmitters. By emulating light-responsive synaptic transmission in the retina, photonic synapses (also called optical or optoelectronic synapses) have been demonstrated using diverse device structures, materials and working mechanisms.<sup>[136–142]</sup> Depending on the illumination condition of a light pulse, photonic synapses have demonstrated various synaptic functions such as short-term sensory and long-term memory responses which can be used for analog-type cognitive image sensors, and for pattern recognition and image learning in neuromorphic computing.<sup>[143–145]</sup> Also, with various materials that have different bandgaps, photonic synapses have demonstrated wavelength selectivity similar to those of cone cells that detect different wavelength of

visible light.<sup>[146–148]</sup> This light selectivity can demonstrate applications with advanced functions such as image recognition,<sup>[149]</sup> optical wireless communication,<sup>[150]</sup> and UV light detection.<sup>[136]</sup>

In phototransistors, photo-induced excessive charge carriers generated from photosensitive materials can be transferred to and captured at trap states in interfaces or semiconductors.<sup>[151]</sup> Photo-induced charges in semiconductors trapped at the interface of the semiconductors/gate insulators can exhibit memory effects.<sup>[152,153]</sup> Gradual filling of charge trapping sites by light-stimulated charges gradually modulates  $V_{\text{th}}$  of the phototransistors. For example, organic photosensitive transistors with polymer gate insulators have been studied in which interfacial effects mediating interaction between polar groups of the polymer dielectric and side chains of organic semiconductors can influence shallow and deep traps on the interfaces; these changes are related to  $\Delta V_{\text{th}}$  and the memory effect.<sup>[154]</sup> Organic transistor composed of a polymer dielectric with a large dipole moment have a strong interfacial effect that enables current potentiation upon stimulation by a pulse of light.<sup>[155]</sup> After illumination, the current relaxes due to release of trapped charges.

Photonic synapses have also showed synaptic plasticity. Rapid changes have been obtained using reversible transfer of photo-induced charges between graphene-carbon nanotube heterogeneous semiconductors.<sup>[156]</sup> Slow changes have been obtained by using gate bias to induce trapping of interface charges. Also, in a Ge-gated  $\text{MoS}_2$  phototransistor, infrared light (wavelength  $\lambda = 1550$  nm) is transmitted through the  $\text{MoS}_2$  semiconductor and  $\text{SiO}_2$  dielectric but absorbed by that Ge gate electrode, where it induces band bending and  $\Delta V_{\text{th}}$ .<sup>[157]</sup> Combined with voltage pulses under illumination, this phototransistor functioned as an optic-neural synapse.

Amorphous metal oxide semiconductors that have inherent persistent photoconductivity have generated photo-induced carriers under UV light illumination (Figure 3b).<sup>[158,159]</sup> Absorption of UV light stimulated band-to-band excitation, ionization of oxygen vacancies and formation of metastable peroxides, so the conductivity of the semiconductors increased (Figure 3c).<sup>[148]</sup> Owing to persistent photoconductivity mainly contributed by ionized oxygen vacancies that require thermal activation energy for neutralization, amorphous metal oxide semiconductors have slow current decay, which is a memory effect (Figure 3d). Layered black phosphorus is easily oxidized in ambient air, and has the unique property that the conductivity decreases under stimulation at  $\lambda = 365$  nm (UV-A), but increases under stimulation at  $\lambda = 280$  nm light (UV-B) without an external electric field.<sup>[160]</sup> Under UV-A, surface-absorbed oxygen induces charge traps in black phosphorus, and this process decreases its conductivity. In contrast, under UV-B, hydrogen molecules dissociate and passivate oxygen sites in oxidized black phosphorus and induce formation of additional carriers, so the conductivity increases. Therefore, current potentiation and depression can be controlled by UV light pulses with different wavelengths.

In floating-gate transistors that use light-sensitive materials in a floating gate layer, photo-activated charge carriers (electrons or holes) are transferred to a semiconducting layer depending on the polarity of electric field, and the remaining charges cause  $\Delta V_{\text{th}}$ .<sup>[161]</sup> Consecutive input of light pulses exploits the memory effect induced by the trapped or stored charges to demonstrate excitatory postsynaptic current (EPSC) by gradual modulation

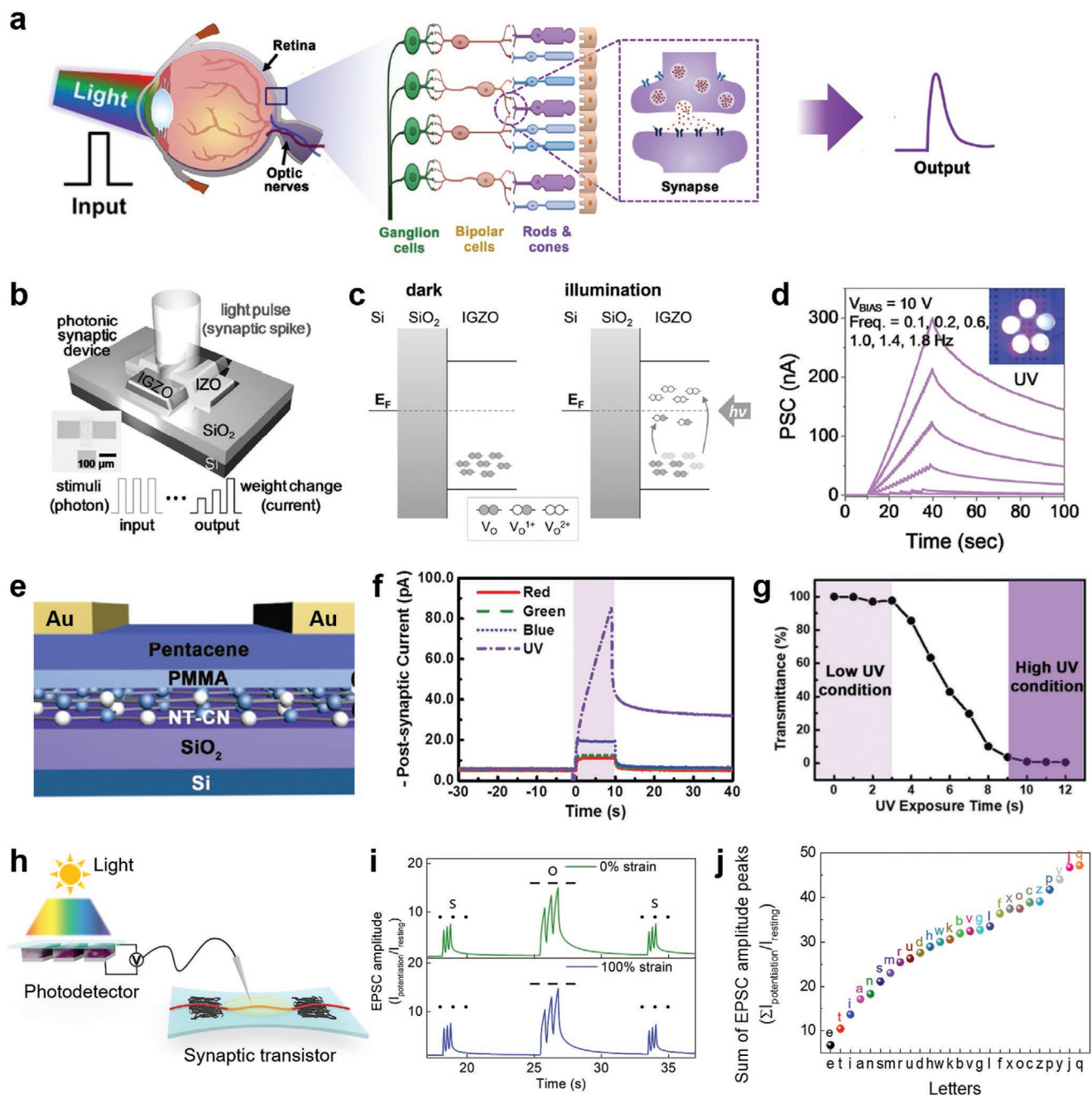


**Figure 3.** Neuromorphic skin with artificial photoreceptors. a) Schematics of the human eye and cellular structure of the retina. Reproduced with permission.<sup>[136]</sup> Copyright 2020, Wiley-VCH. b) Schematic of an artificial synapse that uses an amorphous metal-oxide semiconductor phototransistor. c) Energy band diagrams of a synaptic transistor that uses amorphous indium gallium zinc oxide (IGZO), in darkness and under illumination ( $V_O =$  oxygen vacancies). d) Dependence of postsynaptic current (PSC) responses on UV light frequency in an IGZO synaptic transistor. Reproduced with permission.<sup>[148]</sup> Copyright 2017, Wiley-VCH. e) Schematics of UV-responsive synaptic transistor that uses nitric-acid-treated carbon nitride (NT-CN). f) UV selective response of a synaptic transistor that uses NT-CN. g) Transmittance of UV light in a conceptual smart window integrated with a synaptic transistor and UV transmittance modulator that uses NT-CN, and that detects and blocks UV light. e–g) Reproduced with permission.<sup>[136]</sup> Copyright 2020, Wiley-VCH. h) Schematic of an organic optoelectronic synapse integrated with an external self-powered photodetector and a stretchable organic nanowire synaptic transistor. i) EPSC amplitude responses of a stretchable organic nanowire synaptic transistor triggered by the International Morse code of “SOS” under 0% and 100% strain. j) Linear correlation between the sum of EPSC amplitude peak value and every English letter of the International Morse code. Reproduced under the terms of the Creative Commons CC BY 4.0 License.<sup>[150]</sup> Copyright 2018, The Authors, published by American Association for the Advancement of Science.

of current levels.<sup>[162]</sup> Reverse voltage bias releases trapped or stored charges and returns the  $V_{th}$  to its original state.<sup>[163]</sup>

In floating gated organic transistors that use pentacene semiconductors, the devices control the light selectivity depending

on the light sensitive nanomaterials surrounded by polymer (polymethyl methacrylate, PMMA) in the floating-gate layers (Figure 3e).<sup>[136,164]</sup> For example, CsPbBr<sub>3</sub> quantum dots (QDs) responded to wavelengths  $365 \leq \lambda \leq 660$  nm, and MoSe<sub>2</sub>/Bi<sub>2</sub>Se<sub>3</sub> nanosheets responded to  $580 \leq \lambda \leq 860$  nm.<sup>[164]</sup> In contrast, C<sub>3</sub>N<sub>4</sub> nanodots responded only to  $\lambda = 365$  nm (Figure 3f),<sup>[136]</sup> so they can provide wavelength selectivity for UV ray detection and protection in smart windows (Figure 3g).

External photodetection devices can supply sensory inputs to the connected synaptic devices under illumination. For example, photosensors have been integrated with synaptic transistors in a voltage-divider configuration.<sup>[149,165,166]</sup> They detected light stimuli and modulated voltage bias that is applied to the synaptic transistors. Light-sensory synapses that integrate external sensory devices to synaptic devices have more complicated configuration than photoactive transistors (e.g., phototransistors or light-sensitive floating-gate transistors), but have the advantages that they can use independently well-developed photosensors and synaptic devices.

A photosensor that had a van der Waals (vdW) heterostructure (*h*-BN/WSe<sub>2</sub>) integrated with a charge-trapping synaptic transistor, could detect red ( $\lambda = 655$  nm), green ( $\lambda = 532$  nm), and blue ( $\lambda = 405$  nm) lights.<sup>[149]</sup> An organic photosensor was integrated with an organic ferroelectric/electrochemical synaptic transistor, and demonstrated short-term plasticity and long-term plasticity by electrochemical reaction and ferroelectric dipole switching.<sup>[165]</sup> A metal chalcogenide (CdSe) photosensor integrated with an ionotronic amorphous metal oxide synaptic transistor demonstrated environment-adaptable perception behaviors that may be useful in artificial visual perception systems.<sup>[166]</sup> Self-powered organic (visible light) or silicon (from UV to IR) photodetectors detect light stimuli and transfer sensory inputs to a stretchable organic nanowire synaptic transistor (Figure 3h).<sup>[150]</sup> The stretchable synaptic transistor demonstrated stable synaptic responses under 0% and 100% strain. Light pulses that represented International Morse code induced discrete EPSC responses (Figure 3i) that linearly correlated with every letter of English alphabet individually (Figure 3j). This ability has potential applications in optical wireless communication.

### 3.2. Mechanoreceptors

Mechanoreceptors in skin detect mechanical stimuli such as static and dynamic pressures, stretch, slip and vibration.<sup>[40,132,167–169]</sup> For example, slow-adapting type-I (SA-I) receptors are mechanosensory nerve endings that detect static pressure range (1–80 kilopascals).<sup>[170]</sup> As the strength of the pressure stimulus increases, the SA-I afferent neuron increases its action potential firing within the frequency range of 0–100 Hz, and the neural signals are transferred to the CNS through synapses. Mechanoreceptive sensors including piezoresistive,<sup>[171]</sup> piezocapacitive,<sup>[172]</sup> piezoelectric,<sup>[173]</sup> and triboelectric<sup>[174–176]</sup> sensors have been integrated with artificial synapses and neurons to emulate signal transmission mechanisms in biological afferent nerves (Figure 4a). These approaches will enable advanced skin-inspired electronics for robotic and prosthetic applications.<sup>[177,178]</sup>

The pressure sensors with the pyramidal structures have very high sensitivity because a sharp tip induce a relatively large deformation at low pressure.<sup>[179,180]</sup> In the pyramidal piezoresistive sensor, as pressure increases, the contact area with the underneath the electrode increases and the resistance decreases, so the amplitude of sensory inputs to synaptic devices also increases.<sup>[181]</sup>

One example is an Au-coated micropyramidal pressure sensor in contact with an indium tin oxide (ITO)/polyethylene terephthalate (PET) bottom electrode that was connected to the top electrode of an organic memristor device.<sup>[182]</sup> A  $5 \times 5$  pressure sensor array with fast response (22 ms), high sensitivity ( $6.7 \times 10^7$  kPa<sup>-1</sup>) at low pressure (1–5 kPa) and durability (> 7,000 cycles) was integrated with Nafion organic memristors in which the conductance was gradually controlled by proton migration according to the synaptic input signals. Protons are continuously supplied from air ambient and move through hydrogen bonding of hydrophilic side chains in Nafion. Directions of proton concentration gradient and electric field modulate conductance of the device. Combination of voltage pulses and static pressure that were applied to the pressure sensor, enabled modulation of synaptic plasticity and recognition of written English characters.

Another pyramidal pressure sensor coated with conductive carbon nanotubes transferred sensory input signals to a connected indium tungsten oxide (IWO) synaptic transistor (Figure 4b).<sup>[183]</sup> In the bottom interdigitated electrodes of the pressure sensors, one was connected to voltage supply electrode  $V_{DD}$  and the other was connected to the gate dielectrics of the synaptic transistors by ionic conductive (ion conductivity =  $3 \times 10^{-3}$  S cm<sup>-1</sup>) and stretchable (40% strain) polyvinyl alcohol (PVA) cables. Without pressure, voltage drop at the pressure sensor was almost equal to  $V_{DD}$ . When pressure was applied, the sensor was pressed, its contact area with the substrate increased, so the resistance decreased between the interdigitated electrodes. Then applied voltage caused formation of an EDL in the ionic conducting PVA cables, and the EDL modulated the channel conductance of IWO synaptic transistors. Depending on the polarity of  $V_{DD}$ , synaptic responses were potentiated or depressed. With two pressure sensors connected to one synaptic transistor, spatiotemporal correlation of multiple sensory inputs was demonstrated. When  $V_{DD}$  on the two sensors had same polarity, the synaptic excitation was potentiated, but when the  $V_{DD}$  had opposite polarity, the synaptic excitation was repressed by inhibitory input. These modulations are similar to tactile perception mechanisms in the skin.

Nanogenerators are emerging self-powered devices. They have been used as mechanosensory receptors to detect mechanical stimuli (strain and vibration). A piezoelectric nanogenerator composed of a PVDF-TrFE layer sandwiched between Au electrode layers generated electric signals when subjected to tensile and compressive strains (Figure 4c).<sup>[184]</sup> Tensile and compressive strains induce opposite polarizations of the dipole in the piezoelectric layer, and therefore induce opposite polarity of output signals from nanogenerators. The generated piezopotentials were transferred to ion gel-gated graphene transistor as gate voltage input. Anion accumulation at the interface of ion gel/graphene down-shifted the Fermi level of graphene, so holes became majority charge carriers in the channel.<sup>[184]</sup> In contrast, cation accumulation at the interface up-shifted the Fermi level



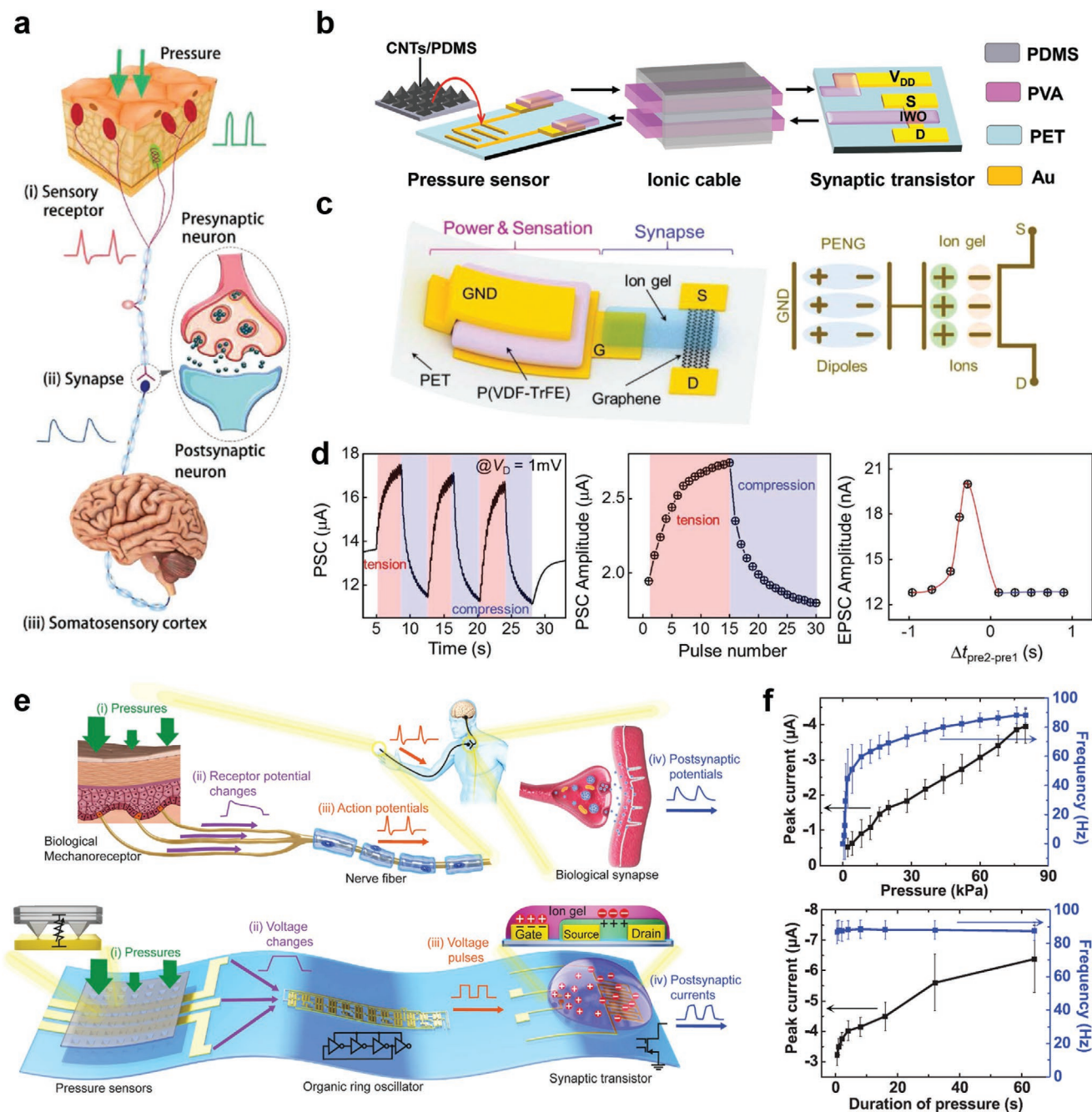


**Figure 4.** Neuromorphic skin with artificial mechanoreceptors. a) Schematics of biological mechanosensory nerve. Reproduced with permission.<sup>[182]</sup> Copyright 2019, Wiley-VCH. b) Schematic of an artificial mechanosensory synapse integrated with a piezoresistive pyramidal pressure sensor, polydimethylsiloxane (PDMS)-encapsulated polyvinyl alcohol (PVA) ionic cables, and an indium tungsten oxide (IWO) synaptic transistor. Reproduced with permission.<sup>[183]</sup> Copyright 2018, Wiley-VCH. c) Schematics of a strain-sensitive artificial synapse composed of a piezoelectric nanogenerator that exploits PVDF-TrFE and an ion gel-gated graphene synaptic transistor. d) PSC modulation under compression and tension strain pulses, PSC amplitude depending on the number of strain pulses, and EPSC amplitude correlated with spatiotemporal strain pulses ( $\Delta t_{\text{pre2-pre1}}$  = interspike interval). Reproduced with permission.<sup>[184]</sup> Copyright 2019, Wiley-VCH. e) Schematics of a biological afferent nerve and an organic artificial afferent nerve. The biological afferent nerve is composed of mechanoreceptors, a nerve fiber, and biological synapses. The organic artificial afferent nerve is composed of pressure sensors, an organic ring oscillator, and synaptic transistors. f) Peak current values and oscillating frequencies of PSC of synaptic transistors depending in the amplitude and duration of pressures. Reproduced with permission.<sup>[170]</sup> Copyright 2018, American Association for the Advancement of Science.

of graphene, so electrons became the majority carriers. In a graphene transistor the Dirac point is slightly shifted to the positive

gate voltage range because of inevitable p-type doping by oxygen and moisture in air ambient conditions. Therefore, within a

certain voltage range between the Dirac point voltage (equivalent to 0.26 V) and 0 V, repetitive compressive strain pulses decreased the conductance in graphene, in a manner similar to an inhibitory response. With repetitive pulses of tensile strain, the channel conductance of graphene transistor increased, similar to an excitatory response. Therefore, an ion gel-gated graphene transistor with two piezoelectric nanogenerators demonstrated dynamic potentiation/depression modulation and spatiotemporal integration of strain information (Figure 4d).

Triboelectric nanogenerators integrated with voltage rectifiers have also been applied to the sensory synapse as mechanosensory receptors for tactile and vibrational stimuli.<sup>[185–187]</sup> A triboelectric nanogenerator composed of Au/amorphous ( $\text{Na}_{0.5}\text{K}_{0.5}$ )  $\text{NbO}_3$  (NKN) platelets/Au was connected to Pt/NKN film/TiN memristors through a bridge rectifier circuit.<sup>[185]</sup> The rectified voltage inputs from the nanogenerator with repetitive tapping induced synaptic potentiation and depression responses. A triboelectric acoustic sensor has been used to demonstrate artificial auditory synapses by connecting with an electrolyte-gated organic synaptic transistor.<sup>[109]</sup> Also, a triboelectric sensory synapse that uses a vibration sensor emulated the spider's mechanical sensory neuron that distinguishes the vibration of cobweb caused by breeze, stronger wind and a fly's struggle.<sup>[186]</sup>

Artificial mechanosensory neurons that convert pressure intensity to action potential firing frequencies can more accurately mimic the biological afferent nerve than sensory synapses in which artificial receptors are directly connected to artificial synapses (Figure 4e).<sup>[170,188]</sup> In the sensory synapses, the number and frequency of touch on the sensor were physically controlled to transmit the presynaptic input to the synapses. In contrast, sensory neurons control the firing frequency of action potentials according to pressure and apply them to synapses.<sup>[170]</sup> A flexible organic ring oscillator and edge detector circuit generated action potentials that had frequency (0–100 Hz) that varied according to the pressure intensity (1–80 kPa) applied to the pyramidal pressure sensor (Figure 4f). The action potentials were transmitted to a flexible electrolyte-gated organic synaptic transistor. The synapse identified the direction of object movement and distinguished Braille letters by integrating sensory signals received from multiple sensors and neuron circuits.

A spiking artificial afferent nerve that used a niobium oxide ( $\text{NbO}_x$ ) memristor protectively inhibited the neuron from excessively high firing rate of action potential when the intensity of stimuli was too strong.<sup>[189]</sup> Within the ordinary range of stimuli intensity, the  $\text{NbO}_x$  memristor increases firing rate with decreased integration time as intensity increases. However, when input signal exceeds the ordinary range, the firing rate decreases because high current flow across the memristor increases relaxation time and induces a large Joule heat that makes the device maintain the 'on' state for a long time. Therefore, when the input signal exceeded the ordinary range, the firing rate decreased. This protective inhibition function is similar to the response of biological neurons to noxious stimuli.

### 3.3. Nociceptors

A nociceptor is a sensory neuron that detects noxious stimuli and then rapidly sends warning signals to the CNS

(Figure 5a).<sup>[190]</sup> When the brain recognizes that the threat exceeds a threshold and may cause damage, a pain alarm is sent to help the body react to the threat and prevent injury.<sup>[191]</sup> Nociception is usually emulated by memristors that exploit electrochemical metallization, because filament forming and abrupt increase of current at voltage above the set voltage are similar to the sensation of pain at such 'suprathreshold' stimuli.<sup>[192–196]</sup> Memristors have emulated four representative nociceptive behaviors: threshold, relaxation, allodynia, and hyperalgesia (Figure 5b).<sup>[192]</sup> A threshold is a certain stimulus intensity at which the nociceptor starts to strongly respond, fires action potentials, and makes pain sensation. After stimuli, the pain slowly decays; this process is relaxation. During relaxation, stimuli with much weaker intensity than the threshold can activate the nociceptor to avoid severe danger. Allodynia is the behavior that after full relaxation, when the nociceptor has been damaged by severe stimuli, it produces a sensation of pain even to subthreshold stimuli.<sup>[193]</sup> Hyperalgesia is the phenomenon that the damaged nociceptor has abnormally increased sensitivity to stimuli and a stronger response to suprathreshold stimuli than the normal nociceptor. The hypersensitive behaviors of damaged nociceptors induce the organism to avoid further risks.

In an artificial nociceptor (memristor), the sensation of pain (output current) increases as the strength (e.g., intensity, period, and interval) of suprathreshold stimuli (voltage) increases.<sup>[194]</sup> The artificial nociceptor in abnormal state generated a high response in the overall stimuli range, including subthreshold and suprathreshold compared to the device in normal state, which are similar to allodynia and hyperalgesia, respectively. Temperature or pressure sensitive nociceptive responses were elicited by using thermoelectric sensory modules to detect temperature stimuli, or piezoelectric sensory modules to detect pressure stimuli (Figure 5c).<sup>[194,195]</sup> As the intensity of temperature or pressure stimuli increased, the responses of the artificial nociceptors increased in magnitude and speed to generate warning signals to prevent further damage (Figure 5d,e).

Although not reviewed here, various sensory synapses that respond to changes in external environment such as sound, chemical, gas, temperature and humidity have been reported.<sup>[197–206]</sup> Therefore, it is expected that various biomimetic sensory systems can be implemented.

## 4. Neuromorphic Skin That Uses Artificial Synapses for Memory and Learning

### 4.1. Memory

The Atkinson-Schiffman model<sup>[207]</sup> of how the brain stores memories suggests that it occurs in three stages: sensory memory (SM), short-term memory (STM), and long-term memory (LTM) (Figure 6a). SM is a step in which external information is stored for a very short time of a few seconds, and is easily forgotten. Information that is not forgotten in the SM stage goes to the STM stage, which maintains the memory for several minutes. To retain the information for a long time, rehearsal must be repeated; this is similar to repetitive learning and memorization. Memory that has been strengthened by repetition passes

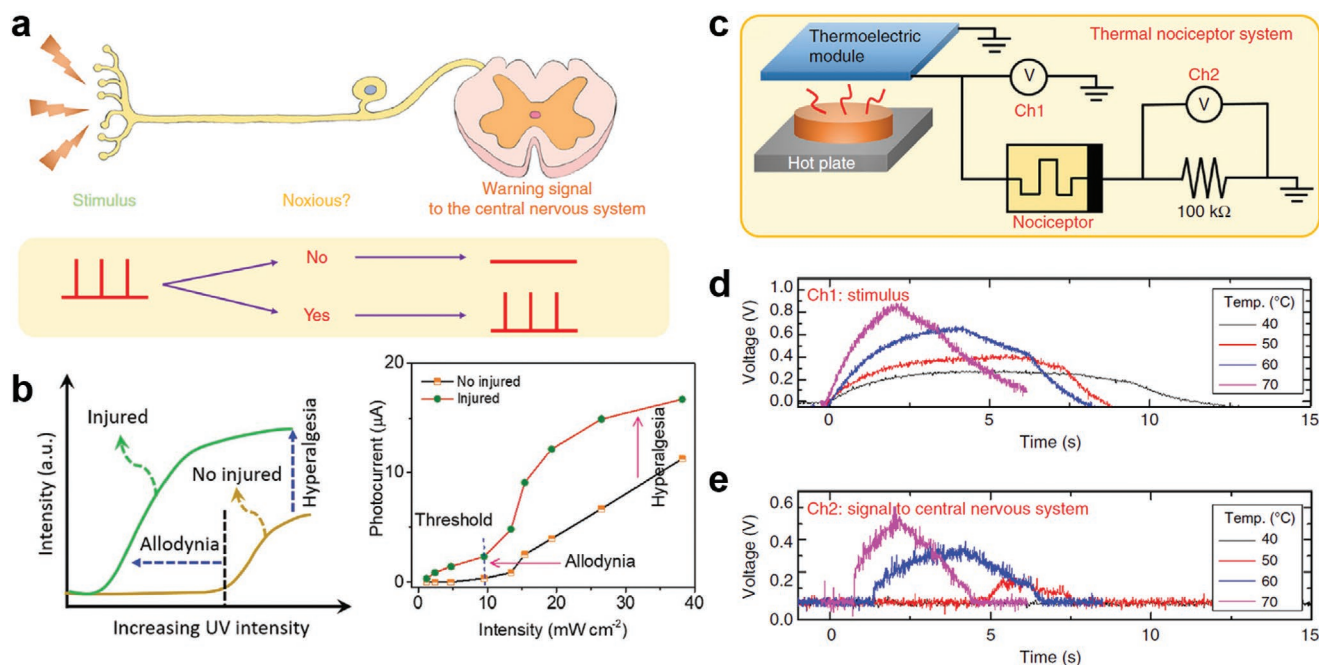


**Figure 5.** Neuromorphic skin with artificial nociceptors. a) Schematics of the biological nociceptive nerve and nociceptive signal transmission mechanism. Reproduced with permission.<sup>[194]</sup> Copyright 2018, Springer Nature. b) Schematic and experimental responses with allodynia and hyperalgesia responses after UV stimuli in normal and damaged photonic nociceptors. Reproduced with permission.<sup>[193]</sup> Copyright 2019, Wiley-VCH. c) Schematic of a thermal nociceptor composed of a thermoelectric module and a memristor. d,e) Voltage outputs from the thermoelectric module measured at d) Ch 1 and voltage responses from on/off switching of the memristor measured at e) Ch 2 depending on temperature. Reproduced with permission.<sup>[194]</sup> Copyright 2018, Springer Nature.

to the LTM, where it is stored for a long time. By imitating the multi-store model of memory, artificial synapses proved that intermittent information is forgotten in the STM stage, but frequent information is maintained for a long time in the LTM stage.<sup>[129,208–210]</sup>

Inorganic Ag<sub>2</sub>S memristive synapse that operates by formation of a conducting bridge of atomic Ag demonstrated multistore model of memory-transition phenomena (Figure 6b). Decay curves of Ag<sub>2</sub>S synapse conductance in STM are analogous to forgetting curves in a brain (Figure 6c).<sup>[208]</sup> Memory retention duration  $\gamma$  decreases as a power function  $\gamma = b \times t^{-m}$ , where  $b$  is a fit constant for scaling,  $t$  is time, and  $m$  is decay rate. As the number of rehearsals increased,  $m$  decreased and memory retention increased.

The STM–LTM transition is dependent on rehearsal repetition frequency. This response has been demonstrated by image memorization in a synapse array. Two images with different rehearsal rates were memorized in a 5 × 5 array of iota-carrageenan (*t*-carrageenan) memristive synapses with metallic filaments (Figure 6d).<sup>[209]</sup> Letter images of “P” shown 10 times at low frequency (67 Hz) and “T” shown 30 times at high frequency (337 Hz) were input to the array. Stimulation with letter image of “P” induced weak conductive filaments in synapses and increased the conductance temporarily. After stimuli, the filaments ruptured quickly and the conductance decayed rapidly. In contrast, the letter image of “T” formed strong filaments in synapses, which that retained the increased conductance for a long time. Sixty seconds after ceasing the inputs of both letter images, only the letter image of “T” was stored in the synapse array (Figure 6e).

Organic memristive synapses can also exploit redox reactions. An organic memristive device composed of an ethyl viologen doperchlorate [EV(ClO<sub>4</sub>)]/triphenylamine-containing polymer (BTFA-F) demonstrated “learning–forgetting–relearning” by emulating the “learning–experience” behavior of human beings (Figure 6f).<sup>[129]</sup> The brain’s LTM decays slowly over time, but relearning can efficiently recover the lost memory. After an initial learning stage composed of 40 stimuli, synaptic weight spontaneously decayed to an intermediate state over time. During the second learning stage, nine stimuli were sufficient to recover the initial synaptic weight. After the second forgetting stage, the third learning stage required only four stimuli to restore the memory state.

The Hebbian learning rule<sup>[211]</sup> describes memory and learning as a consequence of the interactions of nerve cells (the rule of change in synaptic weight). Depending on the activation frequency of connected neurons, the synaptic strength can be increased or decreased. When neurons are activated together repeatedly at a high frequency, the synaptic connection strength between them strengthens, whereas when they are activated intermittently at a low frequency, the synaptic connection strength weakens. This response is described as “cells that fire together, wire together”, and is also related to spike-timing-dependent plasticity (STDP).<sup>[1212]</sup>

Learning and experience strengthen the connections of localized information in the brain, and the information connection is retained for a long-time. Thus, connections between initially unrelated stimuli are strengthened as a consequence of repeated experiences; this phenomenon is called conditioning. Pavlov’s dog experiment is a well-known example of a classical

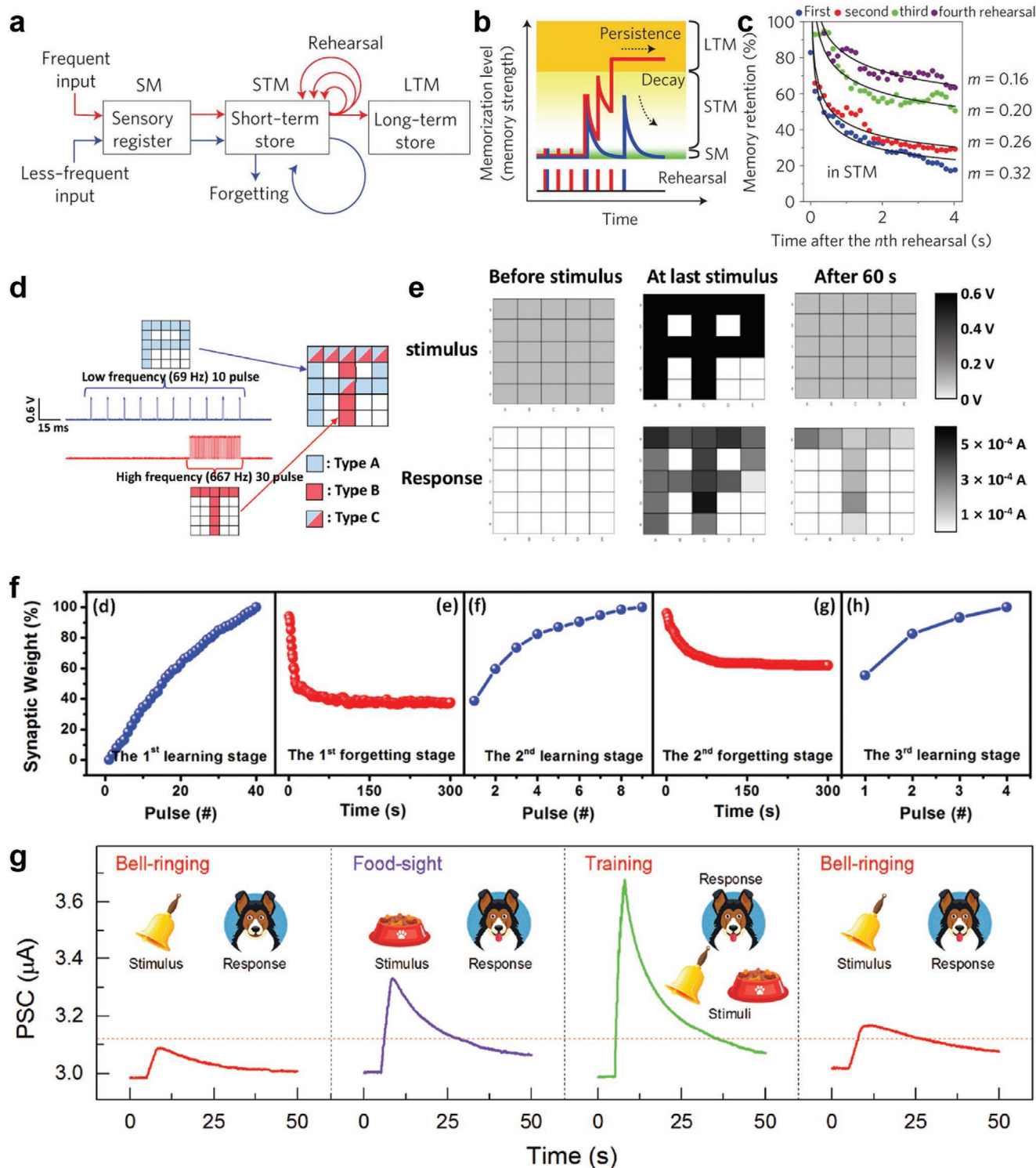


**Figure 6.** Neuromorphic skin for memory. a) The psychological model of human memory proposed by Atkinson and Shiffrin. b) Multistore memorization model in the artificial synapse. c) Memory retention in  $\text{Ag}_2\text{S}$  memristive synapse for decay in STM mode. Reproduced with permission.<sup>[208]</sup> Copyright 2011, Springer Nature. d) Schematic of memorization process of images of letter “P” at a low frequency and “T” at a high frequency using a  $5 \times 5$  array of  $\iota$ -carrageenan memristive synapse array. e) Stimulus and response of  $\iota$ -carrageenan synapse array before stimulus, at the last stimulus, and after 60 s. Reproduced with permission.<sup>[209]</sup> Copyright 2018, American Chemical Society. f) Repeated “learning–forgetting–relearning” processes of a  $\text{EV}(\text{ClO}_4)_2/\text{BTPA-F}$  memristive synapse. Reproduced with permission.<sup>[129]</sup> Copyright 2016, Wiley-VCH. g) The classical conditioning Pavlov’s dog experiment on. Reproduced with permission.<sup>[214]</sup> Copyright 2019, Wiley-VCH.

conditioning that converts a neutral stimulus (NS) to a conditioned stimulus (CS) (Figure 6g).<sup>[213–215]</sup> The sight of food is an unconditioned stimulus (US) for a dog's salivation, which is an unconditioned response (UR). This is the unconditioned reflex. Bell ringing is an NS that elicits no automatic response by the dog. However, after the bell ringing is followed consistently by the sight of food, the bell ringing becomes a CS for the dog's unconscious salivation, before the sight of food; this is a conditioned response (CR). This is a conditioned reflex. Initially, bell ringing did not affect the salivation response, but neural connections in the brain changed to establish a relationship between the stimulus and the (expected) sight of food. These changes in synaptic connection strength according to learning and repeated experiences are instances of Hebbian learning.<sup>[216]</sup>

#### 4.2. Learning

In biological neurons, the soma collects all the information received from the dendrite (Figure 7a). Then the axon hillock fires action potentials when the integrated signals exceed a threshold. The numerous synapses of each dendrite have different synaptic connection strengths according to the activation frequency.<sup>[217]</sup> Therefore, every dendrite transfers different signals depending on the synaptic strengths.

A perceptron is an engineering model of a neuron to develop learning and information-storage models that mimic a brain (Figure 7b).<sup>[218]</sup> The perceptron generates an output that is derived from the inputs, the weight of each input node, the bias, and the activation function. A single-layer perceptron uses a step function as an activation function that resembles the all-or-none law, which is the action potential firing characteristic of a single neuron. The single-layer perceptron can conduct linear classification for one condition such as the Boolean algebra (Binary Logic) of AND, NAND, OR, and NOR gate logic.<sup>[219]</sup> However, the single-layer perceptron cannot solve complex and nonlinear classification conditions (such as XOR), so a multi-layer perceptron with one or more hidden layer, and DNNs that have numerous hidden layers have been developed with nonlinear activation functions.<sup>[220]</sup>

Supervised machine learning use a ground-truth label, which must be provided. The process calculates the estimation error by comparing the output value to the label and with a cost function after a feed-forward process (Figure 7c).<sup>[219,220]</sup> The error is reduced by repeated backpropagation that is guided by the gradient descent of the cost function, which applies partial derivatives and the chain rule in the reverse direction to adjust the weight of the hidden layers.<sup>[221]</sup> Iterative learning minimizes errors by adjusting the weights of nodes in hidden layers. As the number of hidden layers increases, the accuracy of the output value can increase, but the time and energy costs of calculation also increase. In addition, the weight control of many hidden layers during the calculation process can be difficult to interpret.

Although the machine learning with von Neumann computing architecture and learning algorithm, large datasets, and hardware (e.g., GPU) has made strong contributions to realizing the current AI, the process is different from the information processing of the energy-efficient biological NN in the

brain.<sup>[222]</sup> Moreover, the conventional machine learning consumes high time and power costs because a very large amount of data is transferred between the processor and the memory to call and transfer operation instructions and variables during a VMM that requires numerous calculations.<sup>[5]</sup> Use of numerous processors can increase the speed of VMM calculation by running them in parallel, but such computing systems are bulky, heavy and require huge power.<sup>[223]</sup>

As an alternative, a memory network hardware can accelerate the calculation of the VMM in a massively parallel manner by applying Ohm's law and Kirchhoff's current law for multiply-accumulate operations.<sup>[224]</sup> For this purpose, memory devices require linearity and symmetry of continuous conductance states, in addition to non-volatility, high switching speed, low energy consumption, and high endurance.<sup>[225,226]</sup> By using the analog conductance of the memory devices as synaptic weight in an analog VMM, the data movement can be much reduced during the calculation, so the time and power costs can be reduced.

MNIST is a database that has been widely used to evaluate the ability of NNs to undergo supervised learning.<sup>[227]</sup> MNIST consists of  $28 \times 28$  pixel images of handwritten digits, 60 000 for training and 10 000 for testing.<sup>[228]</sup> To test an ANN that uses multilayer perceptrons, each image of  $28 \times 28$  pixels is converted to 784 inputs and transmitted to the input neurons, and through the hidden layers that are composed of fully-connected hidden neurons, then output to the output layer that is composed of 10 neurons that represent digits 0–9.<sup>[229]</sup> The recognition accuracy of the handwriting image character data set varies according to the characteristics of the artificial synapse. For artificial synapses to perform weight calculation and update to analog memory, the synapses should show symmetric and linear modulation of  $>100$  conductance levels with ratio of  $G_{\max}/G_{\min}$  of maximum transconductance to minimum transconductance  $>10$ , and stable cycle-to-cycle and device-to-device stabilities.<sup>[21,105]</sup>

Artificial synapses that use ferroelectric inorganic transistors have 64 conductance states, good linearity (linearity parameters for potentiation  $A_p = -0.8028$  and for depression  $A_d = -0.6979$ ), and  $G_{\max}/G_{\min} = 14.4$  for multiple bias pulses with incremental amplitude (potentiation, 2.7–4.3 V with 25 mV step; depression, –2 to –3.6 V with 25 mV step) (Figure 7d).<sup>[230]</sup> A two-layer perceptron NN that used artificial synapses and had 400 input neurons, 100 hidden neurons, and 10 output neurons achieved an accuracy of 91.1% after 125 training epochs using  $20 \times 20$  MNIST images (Figure 7e). This is comparable to the recognition accuracy of 94.1% obtained using an ideal synaptic NN (Figure 7f). In an endurance test of 100 cycles (12 800 pulse operations), small cycle-to-cycle variation of 2.36% ( $n = 100$  cycles) and device-to-device variation of 3.93% ( $n = 40$  devices) were obtained, and therefore the NN exhibited high recognition accuracy.

To use artificial synapses as an ANN accelerator, they must have low driving voltage, fast switching speed, and low energy consumption. A battery-like organic artificial synapse composed of conducting polymer (PEDOT:PSS) and solid electrolytes (Nafion or ion gel) demonstrated  $\geq 100$  conductance states of potentiation and depression, linear symmetry, cycle uniformity, and long retention when multiple spikes with the same

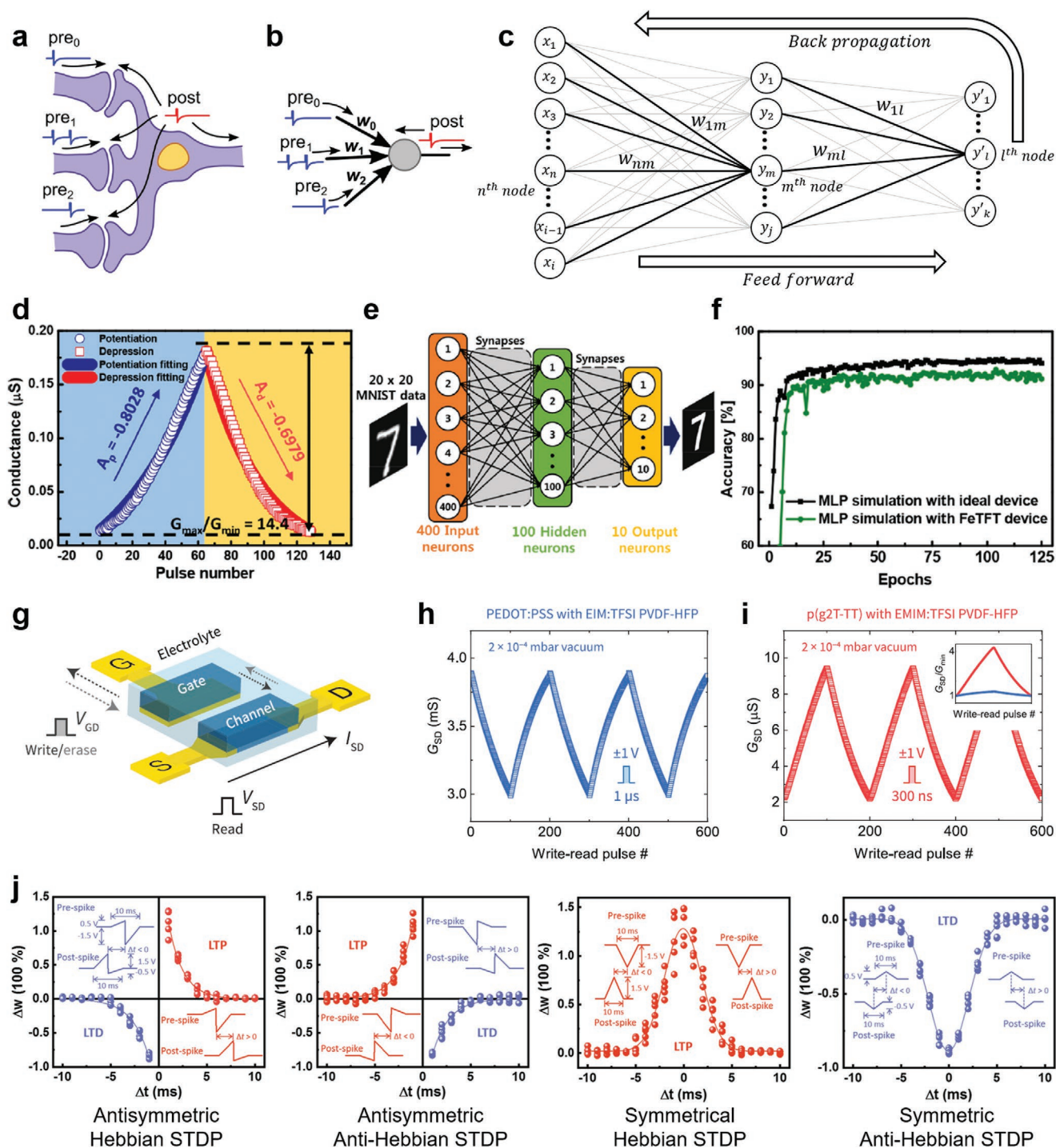


**Figure 7.** Neuromorphic skin for learning. a,b) Schematics of a) biological neuron and b) engineering model of a neuron. Reproduced with permission.<sup>[237]</sup> Copyright 2014, Springer Nature. c) Schematic of fully connected artificial neural network. d) Conductance-state modulation with potentiation and depression responses of a ferroelectric synaptic transistor with ramping voltage pulses. e) Schematic of neural network for MNIST pattern recognition simulation. f) Simulated pattern recognition accuracy of ferroelectric synaptic transistors and an ideal device. Reproduced with permission.<sup>[230]</sup> Copyright 2019, American Chemical Society. g) Schematic of a battery-like organic electrochemical synaptic transistor. h,i) Channel-conductance modulation of battery-like organic electrochemical synaptic transistors with h) conducting polymer (PEDOT:PSS) and ion gel (1-ethylimidazolium bis(trifluoromethylsulfonyl)imide (EIM:TFSI) and PVDF-HFP) and with i) semiconducting polymer (p(g2T-TT)) and ion gel (EMIM:TFSI and PVDF-HFP). Reproduced with permission.<sup>[232]</sup> Copyright 2020, American Association for the Advancement of Science. j) STDP responses of asymmetric Hebbian, asymmetric anti-Hebbian, symmetric Hebbian (LTP), and symmetric anti-Hebbian (LTD). Reproduced with permission.<sup>[241]</sup> Copyright 2019, Wiley-VCH.

amplitude were applied (Figure 7g).<sup>[231,232]</sup> MNIST simulation with the  $28 \times 28$  pixel image dataset showed data recognition accuracy of 97%, which is only 2% lower than obtained using an ideal NN.<sup>[231]</sup> However, when the write pulses are short ( $\approx 1$   $\mu$ s or less), the narrow dynamic range ( $G_{\max}/G_{\min} < 2$ ) was sensitive to device-to-device variations and write noise (Figure 7h).<sup>[232]</sup> The device write noise should be  $< 0.3\%$  of dynamic range.<sup>[233]</sup>

A battery-like organic artificial synapse in which the conducting polymer channel and electrolyte were replaced with a semiconducting polymer (poly(2-(3,3-bis(2-(2-(2-methoxyethoxy)ethoxy)ethoxy)-[2,2-bithiophen]-5-yl)thieno [3,2-b]thiophene) [p(g2T-TT)]) and ion gel (1-ethyl-3-methylimidazolium bis(trifluoromethylsulfonyl)imide (EMIM:TFSI) ionic liquid and poly(vinylidene fluoride-co-hexafluoropropylene) (PVDF-HFP) polymer matrix) had increased dynamic range to  $G_{\max}/G_{\min} > 4$  with 300-ns write pulses ( $\pm 1$  V), and signal-to-noise ratio ( $\Delta G^2/\sigma^2 > 100$ , where  $\Delta G$  is the conductance update and  $\sigma$  is its standard deviation) (Figure 7i).<sup>[232]</sup> By scaling the device to a  $45 \mu\text{m} \times 15 \mu\text{m}$  channel, a device that had  $G_{\max}/G_{\min} > 2$  during  $100 \times 20$ -ns programming pulses ( $\pm 1$  V) consumed  $\approx 80$  fJ/write.

An SNN emulates a biological NN's use of spike rate and spike timing to transmit spatiotemporal information between neurons.<sup>[52]</sup> An SNN has a sparsely-connected structure and processes information by sporadically-delivered voltage spikes, whereas an ANN has a fully-connected structure through hidden layers. Therefore, only specific neurons are activated in an SNN in response to synaptic events, and this arrangement is much more efficient energetically than an ANN, in which all hidden layers of neurons are activated sequentially. Also, an SNN can process data that encodes spatiotemporal information, without the need for additional complex components (e.g., filters in a convolutional NN), so it is advantageous for processing sensory data (image, video, and sound recognition) that encodes spatiotemporal information of the real world.

STDP is an unsupervised learning rule related to LTP and LTD in SNNs.<sup>[234–236]</sup> The synaptic connection between biological neurons strengthens or weakens over the long term, depending on the relative arrival times  $t_{\text{pre}}$  of the input action potential and  $t_{\text{post}}$  of the output action potential. When the input spike occurs just before the output spike ( $\Delta t = t_{\text{pre}} - t_{\text{post}} > 0$ ), the relation between the spikes is likely to be persistently dependent and synchronous, and the synaptic connections between neurons are strengthened on average.<sup>[237]</sup> However, when the input spike occurs immediately after the output spike ( $\Delta t < 0$ ), the correlation between the spikes is likely to be consistently independent and asynchronous, and the connections between neurons are weakened on average. Depending on the sequence and  $\Delta t$  of input and output spikes, as on the neurons and synapses located in different parts of the brain, synaptic weight changes in various forms.<sup>[238,239]</sup>

Numerous artificial synapses have demonstrated the four typical types of STDP response (asymmetric Hebbian, asymmetric anti-Hebbian, symmetric Hebbian, and symmetric anti-Hebbian) (Figure 7j).<sup>[240–245]</sup> Different types of STDP forms can also be implemented by modulating the order,  $\Delta t$ , and shape of input and output spikes.<sup>[246]</sup> For example, two-terminal synapses such as a chalcogenide memristor that uses Ag/AgInSbTe/Ag,<sup>[237]</sup> an inorganic tunnel junction memristor that uses Au/SrTiO<sub>3</sub>/La<sub>0.67</sub>Sr<sub>0.33</sub>MnO<sub>3</sub>,<sup>[241]</sup> and an organic

ferroelectric tunnel junction memristor that uses Au/P(VDF-TrFE)/Nb-doped SrTiO<sub>3</sub><sup>[242]</sup> all showed STDP when pre-spikes were applied to the top electrode and post-spikes were applied to the bottom electrode.

In the asymmetric Hebbian learning rule which is the classical STDP form (initially found in hippocampal cultures), weight updates followed  $\Delta w = A_1 \cdot \exp(-\Delta t/\tau_1)$  ( $\Delta t < 0$ ) and  $\Delta w = A_2 \cdot \exp(\Delta t/\tau_2)$  ( $\Delta t > 0$ ).<sup>[236]</sup> In symmetric STDP, weight updates followed  $\Delta w = A_1 \cdot \exp(-\Delta t^2/(2\tau_1^2))$  and  $\Delta w = A_2 \cdot \exp(-\Delta t^2/(2\tau_2^2))$ .<sup>[242,243]</sup>

In SNN, to demonstrate various STDP forms, additional complex components that modulate the shape of pulses may be required. Also, STDP is a local learning rule, which differ from the error backpropagation in ANN, which uses gradient descent with derivatives. An SNN is event-activated, discontinuous, and sporadically connected, so it is non-differentiable and thereby cannot use backpropagation. Therefore, development of a learning algorithm to be applied to the deep SNN must accompany the development of hardware for it. Also, the learning process is similar to learning rules used in a brain, so an efficient learning process should be sought; clues may be found development of brain science.

## 5. Motion by Neuromorphic Skin That Uses Artificial Synapses

Emulating motor nerves that construct peripheral nerves by connecting with sensory nerves enables interaction with the environment. An artificial motor nerve that mimics the signaling process of a biological motor nerve can make an artificial motor organ move like a biological motor organ.<sup>[150,247–253]</sup> The body motions are mainly generated by sensory perception of external stimuli (e.g., reflex) or intention (e.g., voluntary control).<sup>[254,255]</sup> Unconditioned reflexes occurs when the stimuli received from the sensory nerves and the sensory signals are transmitted directly to the motor nerve through the interneurons in the spinal cord; examples include knee-jerk reflex and withdrawal reflex. In contrast, an conditioned reflex is formed by experience or learning in the brain;<sup>[256]</sup> previously-unrelated stimuli are linked by training; examples include the conditioned Pavlovian reflex in dogs, and motor responses such as an athlete's starting reaction.<sup>[257]</sup> Although conditioned conscious reflexes is more related to the learning in the brain than to strengthening in the motor system, they can become subconscious with practice and offer efficient control of motor response.

Voluntary movements are intentional movement that are not necessarily responses to immediate external stimuli.<sup>[254]</sup> During planning, initiating, and executing of a movement, motor signals are transmitted from the motor cortex to muscle fibers through upper and lower motor neurons. Lower motor neurons are connected to muscle fibers by neuromuscular junctions, which are chemical synapses. The motor signals are transferred from lower motor neurons to muscle fibers via neuromuscular junctions by releasing neurotransmitters in response to action potentials. The actuation of muscle fibers depends on the frequency of the action potentials. After the action potential signals cease, the muscle fibers relax.

Contractions of skeletal muscle fibers can be classified as twitch, summation and tetanus.<sup>[258]</sup> A twitch is a small and temporary contraction of muscle fibers in response to an action potential. Arrival of another action potential before full relaxation of a muscle twitch can induce an additional muscle twitch that is simply summed on the previous twitch. This process resembles signal potentiation in the synapse response. When numerous action potentials stimulate the muscle at high frequency, the contraction of muscle fiber becomes continuous and strong; this response is tetanus.

An artificial neuromuscular junction has been demonstrated using a stretchable organic nanowire transistor that uses an electrolyte (Figure 8a).<sup>[150]</sup> The artificial neuromuscular junction operated a low-voltage-driven polymer actuator, which is an artificial muscle fiber that has a working mechanism similar to that of a biological motor unit. EPSC signals from the stretchable artificial neuromuscular junction were converted to voltage through a transimpedance circuit, then the voltage was applied to the polymer actuator. As voltage increased gradually according to the EPSC response, the polarization of ions inside the polymer actuator gradually increased, so the contraction of the polymer actuator gradually increased (Figure 8b,c). The actuation of the polymer actuator was stable with the stretchable synaptic transistor at 0% or 100% strain.

The muscle contraction is also controlled by recruitment of motor units.<sup>[254]</sup> A motor unit is composed of a lower motor neuron and several muscle fibers that have synaptic connections (neuromuscular junctions). The contraction of the muscle is controlled by activation of motor units that are connected to muscle fibers that are distributed throughout the muscle. When a single motor unit is activated, few muscle fibers are actuated, so the muscle contraction is weak. As the number of recruited motor units increases, the muscle's contraction strengthens. Henneman's size principle suggests that motor units are sequentially recruited from small motor units in which a motor neuron is connected with small number of muscle fibers to a larger motor unit in which a motor neuron is connected to large number of muscle fibers. Therefore, when the neural signals are weak, few motor units are recruited, so contraction is small and slow, but as the strength of the neural signals increases, progressively more motor units are recruited, and the contraction strengthens and accelerates. In this way, motor-unit recruitment will contribute to control the force of artificial muscle contraction along with the development of muscle fibers in future biomimetic motor systems.

A tactile-responsive motor system was implemented using a triboelectric nanogenerator, an electrolytic stretchable rubbery synaptic transistor, and a pneumatic soft robot (Figure 8d).<sup>[247]</sup> Rubbery skins that were composed of triboelectric nanogenerators, rectifiers, and synaptic transistors were integrated on the right, left, and top of the pneumatic robot. The bipolar signals generated from the nanogenerator were rectified to unipolar pulses through the rectifier, then applied to the synapse. The postsynaptic response of the synapse was controlled according to the number of taps on the nanogenerator, then transferred to a programmed control system to control the actuation of the pneumatic robot (Figure 8e).

An artificial reflex arc was implemented using a pyramidal pressure sensor, a flexible memristor, and a polymer actuator

(Figure 8f).<sup>[248]</sup> A memristor that undergoes HRS-to-LRS transition above a certain  $\Delta V_{th}$  was used as a threshold-controlling unit (TCU) to demonstrate a pressure sensory reflex arc that consults an all-or-none law and only fires an action potential when the pressure exceeds a threshold. A memristor that exploited zeolitic imidazolate framework-8 (ZIF-8) was sandwiched between Ag and Au electrodes, and controlled resistance states by forming Ag filaments with  $\Delta V_{th} = 3.5$  V (Figure 8g). When connected to the pyramidal pressure sensor with 4-V bias, HRS-LRS switching occurred when  $\geq 1$  kPa pressure was applied to the sensor (Figure 8h). The grasp reflex response of newborn babies was emulated by controlling a polymer actuator to contract only above a certain pressure (Figure 8i).

A hybrid reflex arc has been demonstrated by connecting an artificial sensory nerve to a biological motor nerve. This result suggested the potential for development of neural prostheses that use neuromorphic electronics (Figure 8j).<sup>[170]</sup> An artificial mechanosensory nerve was connected to biological efferent nerves of a cockroach (*Blaberus discoidalis*) (Figure 8k). The pressure information was converted to postsynaptic signals that eventually induced actuation of the extensor muscle in the leg. According to increase of the intensity and duration of pressure application, the force of leg extension increased (Figure 8l,m). Use of artificial peripheral nerves may increase the compatibility of future neural prostheses that connect to the body, and that operate using biologically-compatible or neurologically-mimetic signals. The artificial peripheral nerves also can be a solution to avoid the huge power consumption of robots that are operated with pneumatics and high voltage.

## 6. Conclusion and Outlook

Over the past few decades, researchers have focused on brain-inspired computing that can process massive amounts of data at low costs of time and power, for use in the future AI era. The hardware called in-memory computing that uses a crossbar memory array has been developed to overcome the von Neumann bottleneck that occurs during deep learning using CMOS digital hardware. A memory crossbar network has been applied in in-memory computing hardware that has analog-like continuous multi-memory states that can effectively calculate VMM by exploiting Ohm's law and Kirchhoff's law.<sup>[259,260]</sup> However, ANNs operate differently from brains that transmit information in the form of voltage spike train. Emulation of brain-like operation might be improved by exploiting knowledge about how the brain works, and by developing learning algorithms for SNNs that transmit and process data that is encoded as voltage spikes.

Development of sensors and robots has focused on improving device abilities such as sensing resolution and applicable force in industrial uses. Future development of humanoid robots, implantable sensors that combine with the human body, wearable exoskeletons, and neural prostheses, will require development of biomimetic electronics and robotics that emulate biological sensory and motor nervous systems. Cognitive sensory and motor systems would enable edge computing and robotics by using voltage spikes to send signals and commands, and to exploit local synaptic plasticity as occurs in



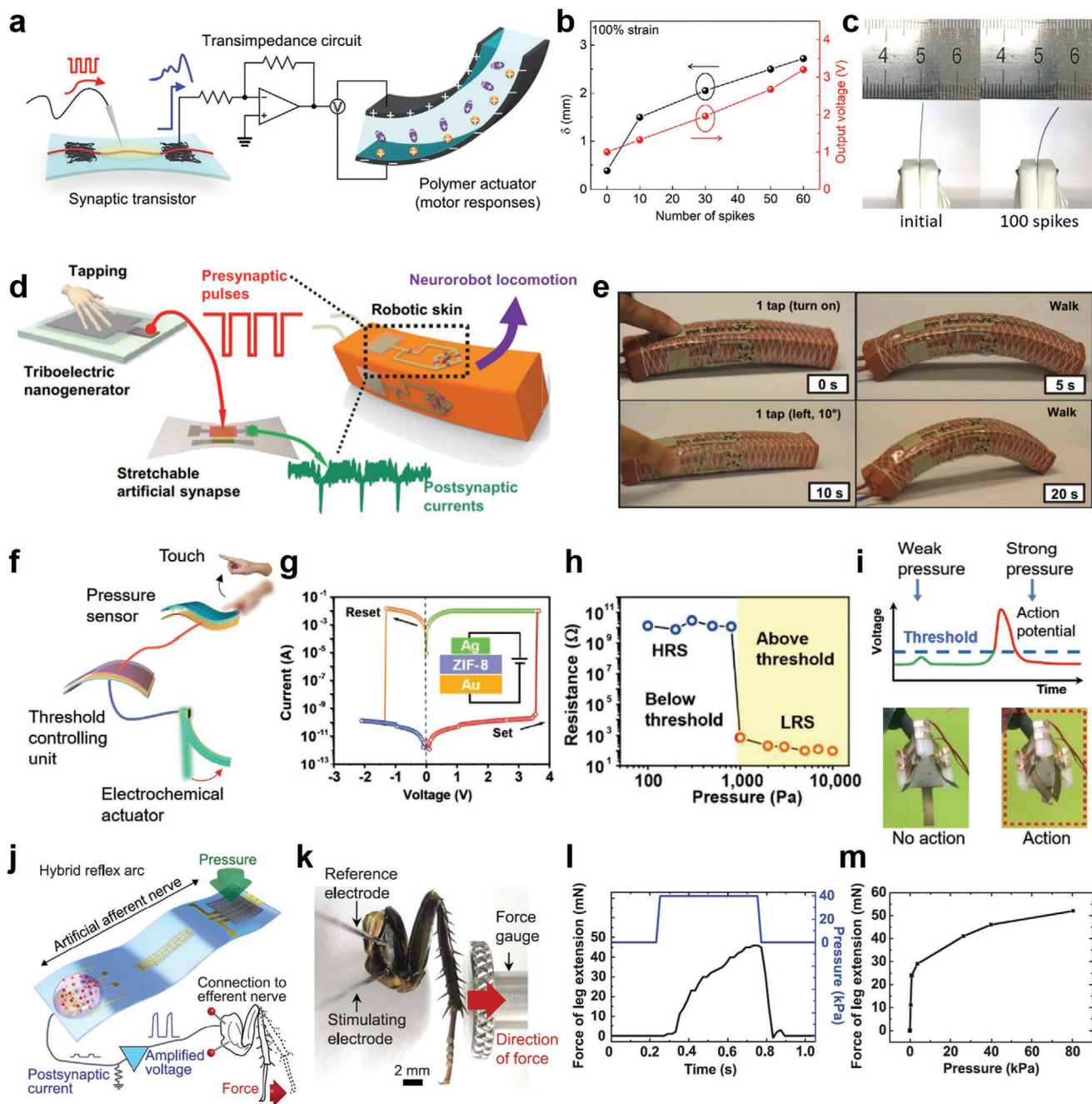


**Figure 8.** Neuromorphic skin for moving. a) Schematic of an artificial neuromuscular junction composed of an electrolytic stretchable organic nanowire synaptic transistor and a polymer actuator. b) Maximum displacement ( $\delta$ ) of the polymer actuator and output voltage generated by the artificial synaptic transistor. c) Digital images of the polymer actuator with 0 and 100 spikes. Reproduced under the terms of the Creative Commons CC BY 4.0 License.<sup>[150]</sup> Copyright 2018, The Authors, published by American Association for the Advancement of Science. d) Schematic of a tactile-responsive motor system implemented with a triboelectric nanogenerator, an electrolytic stretchable rubbery synaptic transistor, and a pneumatic soft robot. e) Digital images of the tactile-responsive soft neurorobot locomotion. Reproduced under the terms of the Creative Commons CC BY 4.0 License.<sup>[247]</sup> Copyright 2019, The Authors, published by American Association for the Advancement of Science. f) An artificial reflex arc integrated with a pyramidal pressure sensor, a flexible ZIF-8 memristor-based threshold controlling unit (TCU), and a polymer actuator. g)  $I$ - $V$  curve of the ZIF-8 memristor (inset: device configuration). h) The resistance change of the TCU depending on the applied pressures. The threshold level of pressure  $\approx$  1 kPa. i) Illustrations that weak pressure below a threshold triggers no action of polymer actuators and the strong pressure above the threshold generates an action potential and triggers action of polymer actuators. Reproduced with permission.<sup>[248]</sup> Copyright 2020, Wiley-VCH. j) Schematic of a hybrid reflex arc connected with an artificial sensory nerve and a biological motor nerve. k) Digital image of a cockroach's leg with the hybrid reflex and a force gauge. l, m) Force of leg extension in response to duration and intensity of pressure on the artificial afferent nerve. Reproduced with permission.<sup>[170]</sup> Copyright 2018, American Association for the Advancement of Science.

biological nervous systems. Artificial synapses that effectively integrate event-stimulated signals from high-density neuromorphic sensors may relieve the burden on microprocessors that periodically scan all pixels. Furthermore, neural prostheses may bypass damaged nerves to connect directly to the living body and deliver biological-analog signals to the brain, sensory and motor nerves, muscles, or to robots. Minimization of the number of circuit elements involved in analog-to-digital signal conversion would enable low-power, biocompatible neural prostheses and health monitoring devices that can replace current digital CMOS devices. For these purposes, the biocompatibility and biomimetic properties of neuromorphic skin devices should be increased by using flexible, stretchable, implantable, and healable materials.

Also, compared to the research on neuromorphic sensory skin that uses spikes to send and process signals, research on artificial muscles and motor systems that operate in this way is lacking, even though biological muscles contract in response to a spike signal. Polymer actuators that operate with low voltage amplitude spikes are frequently used as artificial muscle fibers and their softness is suitable for bioinspired soft robots. However, they may be limited to be used for hard and supportive robots such as robotic limbs and wearable exoskeleton in the current stage. Therefore, the research of more rigid actuators that are driven with spikes is required for artificial motor systems of hard robotics that operate in a biomimetic way.

Recently, neuromorphic circuit that exploits organic synaptic transistors demonstrated robots with functions of sensorimotor integration and learning.<sup>[261]</sup> Organic artificial synapses perform local and decentralized training with real-time feedback in the analog domain, so it relieves the burden on the robotic controller in the digital domain; it would be an example of the hybrid system of neuromorphic skin of emerging artificial synapses integrated with conventional digital robotics.

In addition to the sensory and motor responses and memory/learning, the brain controls hormones that relate to emotion and homeostatic plasticity; the emulation of this function facilitates the demonstration of human-friendly social robots.<sup>[262–265]</sup> Moreover, although this article particularly focuses on emerging artificial synapses for neuromorphic electronics, artificial neurons are another key element for future neuromorphic skin electronics.<sup>[266–271]</sup> In this way, we believe that neuromorphic skin will become a core element in future advanced neuromorphic systems integrated with brain-inspired computing and bioinspired robotics.

## Acknowledgements

Y.L. and J.Y.O. contributed equally to this work. This work was supported by the National Research Foundation of Korea (NRF) grant funded by the Korea government (Ministry of Science and ICT) (NRF-2016R1A3B1908431) and the Creative-Pioneering Researchers Program through Seoul National University (SNU). This work was also supported by the National R&D Program through the National Research Foundation of Korea (NRF) funded by Ministry of Science and ICT (NRF-2021M3F3A2A01037858). Y.L. acknowledges Basic Science Research Program through the National Research Foundation of Korea (NRF) funded by the Ministry of Education (NRF-2021R1A6A3A03038934). J.Y.O. acknowledges National Research Foundation of Korea (NRF)

grant funded by the Korean government (NRF-2021R1C1C1009925, NRF-2020R1A6A1A03048004) and R&D program of the Ministry of Trade, Industry & Energy (Grant Nos. 20016252 and 20015898) funded by the Korea Evaluation Institute of Industrial Technology (KEIT).

## Conflict of Interest

The authors declare no conflict of interest.

## Keywords

artificial nerves, bioinspired electronics, electronic skin, neuromorphic electronics, neuromorphic robotics

Received: February 5, 2022

Revised: April 10, 2022

Published online:

- [1] C. Mead, *Proc. IEEE* **1990**, *78*, 1629.
- [2] C. Black, R. Darie, D. Borton, *Trends Neurosci.* **2018**, *41*, 568.
- [3] Q. Xia, J. J. Yang, *Nat. Mater.* **2019**, *18*, 309.
- [4] E. R. W. van Doremale, P. Gkoupidenis, Y. van de Burgt, *J. Mater. Chem. C* **2019**, *7*, 12754.
- [5] A. Amirsoleimani, F. Alibart, V. Yon, J. Xu, M. R. Pazhouhandeh, S. Ecoffey, Y. Beilliard, R. Genov, D. Drouin, *Adv. Intell. Syst.* **2020**, *2*, 2000115.
- [6] J. Tang, F. Yuan, X. Shen, Z. Wang, M. Rao, Y. He, Y. Sun, X. Li, W. Zhang, Y. Li, B. Gao, H. Qian, G. Bi, S. Song, J. J. Yang, H. Wu, *Adv. Mater.* **2019**, *31*, 1902761.
- [7] A. Sandberg, *arXiv* 2016, *arXiv:1602.04019*.
- [8] Y. Lee, T.-W. Lee, *Acc. Chem. Res.* **2019**, *52*, 964.
- [9] W. Xu, S.-Y. Min, H. Hwang, T.-W. Lee, *Sci. Adv.* **2016**, *2*, 1501326.
- [10] Y. Lee, H.-L. Park, Y. Kim, T.-W. Lee, *Joule* **2021**, *5*, 794.
- [11] F. Rosique, P. J. Navarro, C. Fernández, A. Padilla, *Sensors* **2019**, *19*, 648.
- [12] J. Pei, L. Deng, S. Song, M. Zhao, Y. Zhang, S. Wu, G. Wang, Z. Zou, Z. Wu, W. He, F. Chen, N. Deng, S. Wu, Y. Wang, Y. Wu, Z. Yang, C. Ma, G. Li, W. Han, H. Li, H. Wu, R. Zhao, Y. Xie, L. Shi, *Nature* **2019**, *572*, 106.
- [13] S. Wang, X. Chen, X. Huang, D. Wei Zhang, P. Zhou, *Adv. Intell. Syst.* **2020**, *2*, 2000124.
- [14] A. Stateczny, M. Włodarczyk-Sielicka, P. Burdziakowski, *Sensors* **2021**, *21*, 6586.
- [15] S. Campbell, N. O'Mahony, L. Krpalcova, D. Riordan, J. Walsh, A. Murphy, C. Ryan, *2018 29th Irish Signals and Systems Conf. (ISSC)*, IEEE **2018**, pp. 1–4.
- [16] C. Wang, Z. Yang, S. Wang, P. Wang, C.-Y. Wang, C. Pan, B. Cheng, S.-J. Liang, F. Miao, *Adv. Intell. Syst.* **2020**, *2*, 1900103.
- [17] S. Soman, Jayadeva, M. Suri, *Big Data Anal.* **2016**, *1*, 15.
- [18] O. Krestinskaya, A. P. James, L. O. Chua, *IEEE Trans. Neural Networks Learn. Syst.* **2020**, *31*, 4.
- [19] S. Liu, L. Liu, J. Tang, B. Yu, Y. Wang, W. Shi, *Proc. IEEE* **2019**, *107*, 1697.
- [20] W. Shi, S. Dustdar, *Computer* **2016**, *49*, 78.
- [21] H. Park, Y. Lee, N. Kim, D. Seo, G. Go, T.-W. Lee, *Adv. Mater.* **2020**, *32*, 1903558.
- [22] C. Wan, P. Cai, X. Guo, M. Wang, N. Matsuhisa, L. Yang, Z. Lv, Y. Luo, X. J. Loh, X. Chen, *Nat. Commun.* **2020**, *11*, 4602.
- [23] H. Tan, Y. Zhou, Q. Tao, J. Rosen, S. van Dijken, *Nat. Commun.* **2021**, *12*, 1120.

- [24] F. Sun, Q. Lu, S. Feng, T. Zhang, *ACS Nano* **2021**, *15*, 3875.
- [25] L. Liu, W. Xu, Y. Ni, Z. Xu, B. Cui, J. Liu, H. Wei, W. Xu, *ACS Nano* **2022**, *16*, 2282.
- [26] Y. Wang, Y. Gong, L. Yang, Z. Xiong, Z. Lv, X. Xing, Y. Zhou, B. Zhang, C. Su, Q. Liao, S. Han, *Adv. Funct. Mater.* **2021**, *31*, 2100144.
- [27] J. Yu, X. Yang, G. Gao, Y. Xiong, Y. Wang, J. Han, Y. Chen, H. Zhang, Q. Sun, Z. L. Wang, *Sci. Adv.* **2021**, *7*, eabd9117.
- [28] Y. Liu, M. Pharr, G. A. Salvatore, *ACS Nano* **2017**, *11*, 9614.
- [29] F. Molina-Lopez, T. Z. Gao, U. Kraft, C. Zhu, T. Öhlund, R. Pfattner, V. R. Feig, Y. Kim, S. Wang, Y. Yun, Z. Bao, *Nat. Commun.* **2019**, *10*, 2676.
- [30] S. M. Schmid, M. Hollmann, *Sci. Signaling* **2010**, *3*, pe28.
- [31] A. E. Pereda, *Nat. Rev. Neurosci.* **2014**, *15*, 250.
- [32] T. G. Smart, P. Paoletti, *Cold Spring Harbor Perspect. Biol.* **2012**, *4*, a009662.
- [33] F. O. Schmitt, P. Dev, B. H. Smith, *Science* **1976**, *193*, 114.
- [34] M. Mayford, S. A. Siegelbaum, E. R. Kandel, *Cold Spring Harbor Perspect. Biol.* **2012**, *4*, a005751.
- [35] H. Markram, J. Lübke, M. Frotscher, B. Sakmann, *Science* **1997**, *275*, 213.
- [36] S. M. Dudek, M. F. Bear, *Proc. Natl. Acad. Sci.* **1992**, *89*, 4363.
- [37] D. J. Linden, *Neuron* **1994**, *12*, 457.
- [38] J. Yang, R. Wang, Y. Ren, J. Mao, Z. Wang, Y. Zhou, S. Han, *Adv. Mater.* **2020**, *32*, 2003610.
- [39] G. J. Murphy, *J. Neurosci.* **2004**, *24*, 3023.
- [40] A. Chortos, J. Liu, Z. Bao, *Nat. Mater.* **2016**, *15*, 937.
- [41] P. Zarzecki, *Sensory-Motor Areas and Aspects of Cortical Connectivity, Cerebral Cortex*, Vol. 5, Springer, New York **1986**, pp. 185–215.
- [42] Y. H. Jung, B. Park, J. U. Kim, T. Kim, *Adv. Mater.* **2019**, *31*, 1803637.
- [43] M. Ilami, H. Bagheri, R. Ahmed, E. O. Skowronek, H. Marvi, *Adv. Mater.* **2021**, *33*, 2003139.
- [44] D. Rus, M. T. Tolley, *Nature* **2015**, *521*, 467.
- [45] D. Chen, Q. Pei, *Chem. Rev.* **2017**, *117*, 11239.
- [46] C. Laschi, B. Mazzolai, M. Cianchetti, *Sci. Rob.* **2016**, *1*, eaah3690.
- [47] C. Wan, P. Cai, M. Wang, Y. Qian, W. Huang, X. Chen, *Adv. Mater.* **2020**, *32*, 1902434.
- [48] M. Zhu, T. He, C. Lee, *Appl. Phys. Rev.* **2020**, *7*, 031305.
- [49] D.-G. Seo, G.-T. Go, H.-L. Park, T.-W. Lee, *MRS Bull.* **2021**, *46*, 321.
- [50] M.-K. Kim, Y. Park, I.-J. Kim, J.-S. Lee, *iScience* **2020**, *23*, 101846.
- [51] Y. Li, Z. Wang, R. Midya, Q. Xia, J. J. Yang, *J. Phys. D: Appl. Phys.* **2018**, *51*, 503002.
- [52] A. Sebastian, M. Le Gallo, R. Khaddam-Aljameh, E. Eleftheriou, *Nat. Nanotechnol.* **2020**, *15*, 529.
- [53] J.-S. Lee, *Electron. Mater. Lett.* **2011**, *7*, 175.
- [54] H. Kim, S. Hwang, J. Park, B.-G. Park, *Nanotechnology* **2017**, *28*, 405202.
- [55] M.-S. Lee, J.-W. Lee, C.-H. Kim, B.-G. Park, J.-H. Lee, *IEEE Trans. Electron Devices* **2015**, *62*, 569.
- [56] Y. J. Park, H. T. Kwon, B. Kim, W. J. Lee, D. H. Wee, H.-S. Choi, B.-G. Park, J.-H. Lee, Y. Kim, *IEEE Trans. Electron Devices* **2019**, *66*, 420.
- [57] C.-H. Kim, S. Sung, M.-H. Yoon, *Sci. Rep.* **2016**, *6*, 33355.
- [58] S. Kim, B. Choi, M. Lim, J. Yoon, J. Lee, H.-D. Kim, S.-J. Choi, *ACS Nano* **2017**, *11*, 2814.
- [59] S.-G. Yi, M. U. Park, S. H. Kim, C. J. Lee, J. Kwon, G.-H. Lee, K.-H. Yoo, *ACS Appl. Mater. Interfaces* **2018**, *10*, 31480.
- [60] K. Yang, S. Yuan, Y. Huan, J. Wang, L. Tu, J. Xu, Z. Zou, Y. Zhan, L. Zheng, F. Seoane, *npj Flexible Electron.* **2018**, *2*, 20.
- [61] X. Chen, J. Pan, J. Fu, X. Zhu, C. Zhang, L. Zhou, Y. Wang, Z. Lv, Y. Zhou, S. Han, *Adv. Electron. Mater.* **2018**, *4*, 1800444.
- [62] S. Bhattacharjee, R. Wigchering, H. G. Manning, J. J. Boland, P. K. Hurley, *Sci. Rep.* **2020**, *10*, 12178.
- [63] N. Tiwari, M. Rajput, R. A. John, M. R. Kulkarni, A. C. Nguyen, N. Mathews, *ACS Appl. Mater. Interfaces* **2018**, *10*, 30506.
- [64] F. Alibart, S. Pleutin, D. Guérin, C. Novembre, S. Lenfant, K. Lmimouni, C. Gamrat, D. Vuillaume, *Adv. Funct. Mater.* **2010**, *20*, 330.
- [65] K.-C. Kwon, J.-S. Lee, C. G. Kim, J.-G. Park, *Appl. Phys. Express* **2013**, *6*, 067001.
- [66] Y. Ren, J. Yang, L. Zhou, J. Mao, S. Zhang, Y. Zhou, S. Han, *Adv. Funct. Mater.* **2018**, *28*, 1805599.
- [67] W. Wu, S.-T. Han, S. Venkatesh, Q. Sun, H. Peng, Y. Zhou, C. Yeung, R. K. Y. Li, V. A. L. Roy, *Org. Electron.* **2018**, *59*, 382.
- [68] M. K. Choi, W. K. Kim, S. Sung, C. Wu, H. W. Kim, T. W. Kim, *Sci. Rep.* **2018**, *8*, 12275.
- [69] H. Y. Choi, C. Wu, C. H. Bok, T. W. Kim, *NPG Asia Mater.* **2017**, *9*, 413.
- [70] S.-R. Zhang, L. Zhou, J.-Y. Mao, Y. Ren, J.-Q. Yang, G.-H. Yang, X. Zhu, S.-T. Han, V. A. L. Roy, Y. Zhou, *Adv. Mater. Technol.* **2019**, *4*, 1800342.
- [71] H.-L. Park, T.-W. Lee, *Org. Electron.* **2021**, *98*, 106301.
- [72] A. Sawa, *Mater. Today* **2008**, *11*, 28.
- [73] J. S. Lee, S. Lee, T. W. Noh, *Appl. Phys. Rev.* **2015**, *2*, 031303.
- [74] H. Akinaga, H. Shima, *Proc. IEEE* **2010**, *98*, 2237.
- [75] K. M. Kim, D. S. Jeong, C. S. Hwang, *Nanotechnology* **2011**, *22*, 254002.
- [76] C. Tan, Z. Liu, W. Huang, H. Zhang, *Chem. Soc. Rev.* **2015**, *44*, 2615.
- [77] J. Woo, S. Yu, *IEEE Nanotechnol. Mag.* **2018**, *12*, 36.
- [78] K. Moon, S. Lim, J. Park, C. Sung, S. Oh, J. Woo, J. Lee, H. Hwang, *Faraday Discuss.* **2019**, *213*, 421.
- [79] S. Yu, Y. Wu, R. Jeyasingh, D. Kuzum, H.-S. P. Wong, *IEEE Trans. Electron Devices* **2011**, *58*, 2729.
- [80] M. Wuttig, N. Yamada, *Nat. Mater.* **2007**, *6*, 824.
- [81] H.-S. P. Wong, S. Raoux, S. Kim, J. Liang, J. P. Reifenberg, B. Rajendran, M. Asheghi, K. E. Goodson, *Proc. IEEE* **2010**, *98*, 2201.
- [82] G. W. Burr, M. J. Breitwisch, M. Franceschini, D. Garetto, K. Gopalakrishnan, B. Jackson, B. Kurdi, C. Lam, L. A. Lastras, A. Padilla, B. Rajendran, S. Raoux, R. S. Shenoy, *J. Vac. Sci. Technol., B: Nanotechnol. Microelectron.: Mater., Process., Meas., Phenom.* **2010**, *28*, 223.
- [83] D. Kuzum, R. G. D. Jeyasingh, B. Lee, H.-S. P. Wong, *Nano Lett.* **2012**, *12*, 2179.
- [84] M. Xu, X. Mai, J. Lin, W. Zhang, Y. Li, Y. He, H. Tong, X. Hou, P. Zhou, X. Miao, *Adv. Funct. Mater.* **2020**, *30*, 2003419.
- [85] S. La Barbera, D. R. B. Ly, G. Navarro, N. Castellani, O. Cueto, G. Bourgeois, B. De Salvo, E. Nowak, D. Querlioz, E. Vianello, *Adv. Electron. Mater.* **2018**, *4*, 1800223.
- [86] V. Garcia, M. Bibes, *Nat. Commun.* **2014**, *5*, 4289.
- [87] N. Setter, D. Damjanovic, L. Eng, G. Fox, S. Gevorgian, S. Hong, A. Kingon, H. Kohlstedt, N. Y. Park, G. B. Stephenson, I. Stolitchnov, A. K. Tagansteu, D. V. Taylor, T. Yamada, S. Streiffer, *J. Appl. Phys.* **2006**, *100*, 051606.
- [88] Z. Wen, D. Wu, *Adv. Mater.* **2019**, *32*, 1904123.
- [89] S. Majumdar, B. Chen, Q. H. Qin, H. S. Majumdar, S. van Dijken, *Adv. Funct. Mater.* **2018**, *28*, 1703273.
- [90] A. Chanthbouala, V. Garcia, R. O. Cherifi, K. Bouzehouane, S. Fusil, X. Moya, S. Xavier, H. Yamada, C. Deranlot, N. D. Mathur, M. Bibes, A. Barthélémy, J. Grollier, *Nat. Mater.* **2012**, *11*, 860.
- [91] S. Boyn, J. Grollier, G. Lecerf, B. Xu, N. Locatelli, S. Fusil, S. Girod, C. Carrétéro, K. Garcia, S. Xavier, J. Tomas, L. Bellaiche, M. Bibes, A. Barthélémy, S. Saïghi, V. Garcia, *Nat. Commun.* **2017**, *8*, 14736.
- [92] L. Chen, T.-Y. Wang, Y.-W. Dai, M.-Y. Cha, H. Zhu, Q.-Q. Sun, S.-J. Ding, P. Zhou, L. Chua, D. W. Zhang, *Nanoscale* **2018**, *10*, 15826.
- [93] H. Ryu, H. Wu, F. Rao, W. Zhu, *Sci. Rep.* **2019**, *9*, 20383.
- [94] J. Müller, T. S. Böschke, U. Schröder, S. Mueller, D. Bräuhäus, U. Böttger, L. Frey, T. Mikolajick, *Nano Lett.* **2012**, *12*, 4318.

- [95] J. Muller, T. S. Boscke, S. Muller, E. Yurchuk, P. Polakowski, J. Paul, D. Martin, T. Schenk, K. Khullar, A. Kersch, W. Weinreich, S. Riedel, K. Seidel, A. Kumar, T. M. Arruda, S. V. Kalinin, T. Schlosser, R. Boschke, R. van Bentum, U. Schroder, T. Mikolajick, 2013 *IEEE Int. Electron Devices Meeting*, IEEE **2013**, pp. 10.8.1–10.8.4.
- [96] M.-K. Kim, I.-J. Kim, J.-S. Lee, *Sci. Adv.* **2021**, 7, eabe1341.
- [97] S. Oh, T. Kim, M. Kwak, J. Song, J. Woo, S. Jeon, I. K. Yoo, H. Hwang, *IEEE Electron Device Lett.* **2017**, 38, 732.
- [98] M. Jerry, S. Dutta, A. Kazemi, K. Ni, J. Zhang, P.-Y. Chen, P. Sharma, S. Yu, X. S. Hu, M. Niemier, S. Datta, *J. Phys. D: Appl. Phys.* **2018**, 51, 434001.
- [99] Y. Choi, J.-H. Kim, C. Qian, J. Kang, M. C. Hersam, J.-H. Park, J. H. Cho, *ACS Appl. Mater. Interfaces* **2020**, 12, 4707.
- [100] B. Tian, L. Liu, M. Yan, J. Wang, Q. Zhao, N. Zhong, P. Xiang, L. Sun, H. Peng, H. Shen, T. Lin, B. Dkhil, X. Meng, J. Chu, X. Tang, C. Duan, *Adv. Electron. Mater.* **2019**, 5, 1800600.
- [101] S. Jang, S. Yu, E.-H. Lee, M. Kang, G. Wang, T.-W. Kim, *ACS Appl. Mater. Interfaces* **2019**, 11, 1071.
- [102] A. Chen, *Solid-State Electron.* **2016**, 125, 25.
- [103] E. J. Fuller, F. El Gabaly, F. Léonard, S. Agarwal, S. J. Plimpton, R. B. Jacobs-Gedrim, C. D. James, M. J. Marinella, A. A. Talin, *Adv. Mater.* **2017**, 29, 1604310.
- [104] Y. Tuchman, T. N. Mangoma, P. Gkoupidenis, Y. van de Burgt, R. A. John, N. Mathews, S. E. Shaheen, R. Daly, G. G. Malliaras, A. Salleo, *MRS Bull.* **2020**, 45, 619.
- [105] Y. van de Burgt, A. Melianas, S. T. Keene, G. Malliaras, A. Salleo, *Nat. Electron.* **2018**, 1, 386.
- [106] A. Gumyusenge, A. Melianas, S. T. Keene, A. Salleo, *Annu. Rev. Mater. Res.* **2021**, 51, 47.
- [107] S. Chen, A. Surendran, X. Wu, S. Y. Lee, M. Stephen, W. L. Leong, *Adv. Mater. Technol.* **2020**, 5, 2000523.
- [108] J. Rivnay, S. Inal, A. Salleo, R. M. Owens, M. Berggren, G. G. Malliaras, *Nat. Rev. Mater.* **2018**, 3, 17086.
- [109] D.-G. Seo, Y. Lee, G.-T. Go, M. Pei, S. Jung, Y. H. Jeong, W. Lee, H.-L. Park, S.-W. Kim, H. Yang, C. Yang, T.-W. Lee, *Nano Energy* **2019**, 65, 104035.
- [110] S. Dai, Y. Wang, J. Zhang, Y. Zhao, F. Xiao, D. Liu, T. Wang, J. Huang, *ACS Appl. Mater. Interfaces* **2018**, 10, 39983.
- [111] L. Q. Zhu, C. J. Wan, P. Q. Gao, Y. H. Liu, H. Xiao, J. C. Ye, Q. Wan, *ACS Appl. Mater. Interfaces* **2016**, 8, 21770.
- [112] Y. H. Liu, L. Q. Zhu, P. Feng, Y. Shi, Q. Wan, *Adv. Mater.* **2015**, 27, 5599.
- [113] P. Gkoupidenis, N. Schaefer, B. Garlan, G. G. Malliaras, *Adv. Mater.* **2015**, 27, 7176.
- [114] S. T. Keene, A. Melianas, Y. van de Burgt, A. Salleo, *Adv. Electron. Mater.* **2019**, 5, 1800686.
- [115] E. J. Fuller, S. T. Keene, A. Melianas, Z. Wang, S. Agarwal, Y. Li, Y. Tuchman, C. D. James, M. J. Marinella, J. J. Yang, A. Salleo, A. A. Talin, *Science* **2019**, 364, 570.
- [116] J. Zhu, Y. Yang, R. Jia, Z. Liang, W. Zhu, Z. U. Rehman, L. Bao, X. Zhang, Y. Cai, L. Song, R. Huang, *Adv. Mater.* **2018**, 30, 1800195.
- [117] M. T. Sharbati, Y. Du, J. Torres, N. D. Ardolino, M. Yun, F. Xiong, *Adv. Mater.* **2018**, 30, 1802353.
- [118] X. Zhu, D. Li, X. Liang, W. D. Lu, *Nat. Mater.* **2019**, 18, 141.
- [119] G.-T. Go, Y. Lee, D.-G. Seo, M. Pei, W. Lee, H. Yang, T.-W. Lee, *Adv. Intell. Syst.* **2020**, 2, 2000012.
- [120] Y. Fu, L. Kong, Y. Chen, J. Wang, C. Qian, Y. Yuan, J. Sun, Y. Gao, Q. Wan, *ACS Appl. Mater. Interfaces* **2018**, 10, 26443.
- [121] J. Lenz, F. del Giudice, F. R. Geisenhof, F. Winterer, R. T. Weitz, *Nat. Nanotechnol.* **2019**, 14, 579.
- [122] T.-S. Kim, Y. Lee, W. Xu, Y. H. Kim, M. Kim, S.-Y. Min, T. H. Kim, H. W. Jang, T.-W. Lee, *Nano Energy* **2019**, 58, 437.
- [123] J. J. Yang, Q. Xia, *Nat. Mater.* **2017**, 16, 396.
- [124] T.-L. Choi, K.-H. Lee, W.-J. Joo, S. Lee, T.-W. Lee, M. Y. Chae, *J. Am. Chem. Soc.* **2007**, 129, 9842.
- [125] B. Zhang, F. Fan, W. Xue, G. Liu, Y. Fu, X. Zhuang, X.-H. Xu, J. Gu, R.-W. Li, Y. Chen, *Nat. Commun.* **2019**, 10, 736.
- [126] W. Zhang, C. Wang, G. Liu, X. Zhu, X. Chen, L. Pan, H. Tan, W. Xue, Z. Ji, J. Wang, Y. Chen, R.-W. Li, *Chem. Commun.* **2014**, 50, 11856.
- [127] X. Yang, C. Wang, J. Shang, C. Zhang, H. Tan, X. Yi, L. Pan, W. Zhang, F. Fan, Y. Liu, Y. Chen, G. Liu, R.-W. Li, *RSC Adv.* **2016**, 6, 25179.
- [128] C. Zhang, Y.-T. Tai, J. Shang, G. Liu, K.-L. Wang, C. Hsu, X. Yi, X. Yang, W. Xue, H. Tan, S. Guo, L. Pan, R.-W. Li, *J. Mater. Chem. C* **2016**, 4, 3217.
- [129] G. Liu, C. Wang, W. Zhang, L. Pan, C. Zhang, X. Yang, F. Fan, Y. Chen, R.-W. Li, *Adv. Electron. Mater.* **2016**, 2, 1500298.
- [130] Q. Zhao, Y. Wang, H. Cui, X. Du, *J. Mater. Chem. C* **2019**, 7, 6493.
- [131] Y. Liu, K. He, G. Chen, W. R. Leow, X. Chen, *Chem. Rev.* **2017**, 117, 12893.
- [132] I. You, D. G. Mackanic, N. Matsuhisa, J. Kang, J. Kwon, L. Beker, J. Mun, W. Suh, T. Y. Kim, J. B.-H. Tok, Z. Bao, U. Jeong, *Science* **2020**, 370, 961.
- [133] V. K. Kukkala, J. Tunnell, S. Pasricha, T. Bradley, *IEEE Consum. Electron. Mag.* **2018**, 7, 18.
- [134] K.-N. Kim, M.-J. Sung, H.-L. Park, T.-W. Lee, *Adv. Electron. Mater.* **2022**, 8, 2100935.
- [135] M. Zeng, Y. He, C. Zhang, Q. Wan, *Front. Neurosci.* **2021**, 15, 690950.
- [136] H. Park, H. Kim, D. Lim, H. Zhou, Y. Kim, Y. Lee, S. Park, T.-W. Lee, *Adv. Mater.* **2020**, 32, 1906899.
- [137] G. J. Lee, C. Choi, D. Kim, Y. M. Song, *Adv. Funct. Mater.* **2018**, 28, 1705202.
- [138] J. Mao, L. Zhou, X. Zhu, Y. Zhou, S. Han, *Adv. Opt. Mater.* **2019**, 7, 1900766.
- [139] D. Berco, D. Shenp Ang, *Adv. Intell. Syst.* **2019**, 1, 1900003.
- [140] J. Zhang, S. Dai, Y. Zhao, J. Zhang, J. Huang, *Adv. Intell. Syst.* **2020**, 2, 1900136.
- [141] F. Zhou, J. Chen, X. Tao, X. Wang, Y. Chai, *Research* **2019**, 2019, 9490413.
- [142] M. S. Kim, M. S. Kim, G. J. Lee, S. Sunwoo, S. Chang, Y. M. Song, D. Kim, *Adv. Mater. Technol.* **2022**, 7, 2100144.
- [143] H. Jang, C. Liu, H. Hinton, M. Lee, H. Kim, M. Seol, H. Shin, S. Park, D. Ham, *Adv. Mater.* **2020**, 32, 2002431.
- [144] F. Zhou, Z. Zhou, J. Chen, T. H. Choy, J. Wang, N. Zhang, Z. Lin, S. Yu, J. Kang, H.-S. P. Wong, Y. Chai, *Nat. Nanotechnol.* **2019**, 14, 776.
- [145] C. Zhang, F. Xu, X. Zhao, M. Zhang, W. Han, H. Yu, S. Wang, Y. Yang, Y. Tong, Q. Tang, Y. Liu, *Nano Energy* **2022**, 95, 107001.
- [146] S. Gao, G. Liu, H. Yang, C. Hu, Q. Chen, G. Gong, W. Xue, X. Yi, J. Shang, R.-W. Li, *ACS Nano* **2019**, 13, acsnano.9b00340.
- [147] J. J. Yu, L. Y. Liang, L. X. Hu, H. X. Duan, W. H. Wu, H. L. Zhang, J. H. Gao, F. Zhuge, T. C. Chang, H. T. Cao, *Nano Energy* **2019**, 62, 772.
- [148] M. Lee, W. Lee, S. Choi, J.-W. Jo, J. Kim, S. K. Park, Y.-H. Kim, *Adv. Mater.* **2017**, 29, 1700951.
- [149] S. Seo, S.-H. Jo, S. Kim, J. Shim, S. Oh, J.-H. Kim, K. Heo, J.-W. Choi, C. Choi, S. Oh, D. Kuzum, H.-S. P. Wong, J.-H. Park, *Nat. Commun.* **2018**, 9, 5106.
- [150] Y. Lee, J. Y. Oh, W. Xu, O. Kim, T. R. Kim, J. Kang, Y. Kim, D. Son, J. B.-H. Tok, M. J. Park, Z. Bao, T.-W. Lee, *Sci. Adv.* **2018**, 4, eaat7387.
- [151] K.-J. Baeg, M. Binda, D. Natali, M. Caironi, Y.-Y. Noh, *Adv. Mater.* **2013**, 25, 4267.
- [152] Y. B. Guo, L. Q. Zhu, W. T. Gao, Z. Y. Ren, H. Xiao, Z. Y. Ge, *Org. Electron.* **2019**, 71, 31.
- [153] Y. Zhong, X. Gao, J. Xu, H. Sirringhaus, S. Wang, *Adv. Electron. Mater.* **2020**, 6, 1900955.

- [154] X. Wu, Y. Chu, R. Liu, H. E. Katz, J. Huang, *Adv. Sci.* **2017**, *4*, 1700442.
- [155] S. Dai, X. Wu, D. Liu, Y. Chu, K. Wang, B. Yang, J. Huang, *ACS Appl. Mater. Interfaces* **2018**, *10*, 21472.
- [156] S. Qin, F. Wang, Y. Liu, Q. Wan, X. Wang, Y. Xu, Y. Shi, X. Wang, R. Zhang, *2D Mater.* **2017**, *4*, 035022.
- [157] S.-G. Kim, S.-H. Kim, J. Park, G.-S. Kim, J.-H. Park, K. C. Saraswat, J. Kim, H.-Y. Yu, *ACS Nano* **2019**, *13*, 10294.
- [158] Y. Chen, W. Qiu, X. Wang, W. Liu, J. Wang, G. Dai, Y. Yuan, Y. Gao, J. Sun, *Nano Energy* **2019**, *62*, 393.
- [159] W. Alquraishi, Y. Fu, W. Qiu, J. Wang, Y. Chen, L.-A. Kong, J. Sun, Y. Gao, *Org. Electron.* **2019**, *71*, 72.
- [160] T. Ahmed, S. Kuriakose, S. Abbas, M. J. S. Spencer, M. A. Rahman, M. Tahir, Y. Lu, P. Sonar, V. Bansal, M. Bhaskaran, S. Sriram, S. Walia, *Adv. Funct. Mater.* **2019**, *29*, 1901991.
- [161] J. Sun, S. Oh, Y. Choi, S. Seo, M. J. Oh, M. Lee, W. B. Lee, P. J. Yoo, J. H. Cho, J.-H. Park, *Adv. Funct. Mater.* **2018**, *28*, 1804397.
- [162] Y. Wang, J. Yang, W. Ye, D. She, J. Chen, Z. Lv, V. A. L. Roy, H. Li, K. Zhou, Q. Yang, Y. Zhou, S. Han, *Adv. Electron. Mater.* **2020**, *6*, 1900765.
- [163] J.-Y. Mao, L. Hu, S.-R. Zhang, Y. Ren, J.-Q. Yang, L. Zhou, Y.-J. Zeng, Y. Zhou, S.-T. Han, *J. Mater. Chem. C* **2019**, *7*, 48.
- [164] Y. Wang, Z. Lv, J. Chen, Z. Wang, Y. Zhou, L. Zhou, X. Chen, S.-T. Han, *Adv. Mater.* **2018**, *30*, 1802883.
- [165] H. Wang, Q. Zhao, Z. Ni, Q. Li, H. Liu, Y. Yang, L. Wang, Y. Ran, Y. Guo, W. Hu, Y. Liu, *Adv. Mater.* **2018**, *30*, 1803961.
- [166] S. M. Kwon, S. W. Cho, M. Kim, J. S. Heo, Y. Kim, S. K. Park, *Adv. Mater.* **2019**, *31*, 1906433.
- [167] H. Pan, T.-W. Lee, *Adv. Healthcare Mater.* **2021**, *10*, 2100460.
- [168] B. C.-K. Tee, A. Chortos, A. Berndt, A. K. Nguyen, A. Tom, A. McGuire, Z. C. Lin, K. Tien, W.-G. Bae, H. Wang, P. Mei, H.-H. Chou, B. Cui, K. Deisseroth, T. N. Ng, Z. Bao, *Science* **2015**, *350*, 313.
- [169] S. Chun, J.-S. Kim, Y. Yoo, Y. Choi, S. J. Jung, D. Jang, G. Lee, K.-I. Song, K. S. Nam, I. Youn, D. Son, C. Pang, Y. Jeong, H. Jung, Y.-J. Kim, B.-D. Choi, J. Kim, S.-P. Kim, W. Park, S. Park, *Nat. Electron.* **2021**, *4*, 429.
- [170] Y. Kim, A. Chortos, W. Xu, Y. Liu, J. Y. Oh, D. Son, J. Kang, A. M. Foudeh, C. Zhu, Y. Lee, S. Niu, J. Liu, R. Pfaltner, Z. Bao, T.-W. Lee, *Science* **2018**, *360*, 998.
- [171] X. Wang, Z. Zhou, C. Ban, Z. Zhang, S. Ju, X. Huang, H. Mao, Q. Chang, Y. Yin, M. Song, S. Cheng, Y. Ding, Z. Liu, R. Ju, L. Xie, F. Miao, J. Liu, W. Huang, *Adv. Sci.* **2020**, *7*, 1902864.
- [172] Y. Zang, H. Shen, D. Huang, C.-A. Di, D. Zhu, *Adv. Mater.* **2017**, *29*, 1606088.
- [173] M. Kumar, J. Kim, C.-P. Wong, *Nano Energy* **2019**, *63*, 103843.
- [174] Y. Liu, J. Zhong, E. Li, H. Yang, X. Wang, D. Lai, H. Chen, T. Guo, *Nano Energy* **2019**, *60*, 377.
- [175] C. Wu, T. W. Kim, J. H. Park, B. Koo, S. Sung, J. Shao, C. Zhang, Z. L. Wang, *ACS Nano* **2020**, *14*, 1390.
- [176] J. Yu, G. Gao, J. Huang, X. Yang, J. Han, H. Zhang, Y. Chen, C. Zhao, Q. Sun, Z. L. Wang, *Nat. Commun.* **2021**, *12*, 1581.
- [177] K. Lee, S. Huang, M. Tsai, S. Yang, C. Lin, M. Li, Y.-M. Chang, K. Watanabe, T. Taniguchi, Y.-C. Lai, S.-P. Lin, P. Chiu, Y.-F. Lin, *Matter* **2021**, *4*, 1598.
- [178] X. Liao, W. Song, X. Zhang, C. Yan, T. Li, H. Ren, C. Liu, Y. Wang, Y. Zheng, *Nat. Commun.* **2020**, *11*, 268.
- [179] H.-H. Chou, A. Nguyen, A. Chortos, J. W. F. To, C. Lu, J. Mei, T. Kurosawa, W.-G. Bae, J. B.-H. Tok, Z. Bao, *Nat. Commun.* **2015**, *6*, 8011.
- [180] C.-L. Choong, M.-B. Shim, B.-S. Lee, S. Jeon, D.-S. Ko, T.-H. Kang, J. Bae, S. H. Lee, K.-E. Byun, J. Im, Y. J. Jeong, C. E. Park, J.-J. Park, U.-I. Chung, *Adv. Mater.* **2014**, *26*, 3451.
- [181] Z. Huang, M. Gao, Z. Yan, T. Pan, S. A. Khan, Y. Zhang, H. Zhang, Y. Lin, *Sens. Actuators, A* **2017**, *266*, 345.
- [182] C. Zhang, W. Bin Ye, K. Zhou, H. Chen, J. Yang, G. Ding, X. Chen, Y. Zhou, L. Zhou, F. Li, S. Han, *Adv. Funct. Mater.* **2019**, *29*, 1808783.
- [183] C. Wan, G. Chen, Y. Fu, M. Wang, N. Matsuhisa, S. Pan, L. Pan, H. Yang, Q. Wan, L. Zhu, X. Chen, *Adv. Mater.* **2018**, *30*, 1801291.
- [184] Y. Chen, G. Gao, J. Zhao, H. Zhang, J. Yu, X. Yang, Q. Zhang, W. Zhang, S. Xu, J. Sun, Y. Meng, Q. Sun, *Adv. Funct. Mater.* **2019**, *29*, 1900959.
- [185] B.-Y. Kim, H.-G. Hwang, J.-U. Woo, W.-H. Lee, T.-H. Lee, C.-Y. Kang, S. Nahm, *NPG Asia Mater.* **2017**, *9*, 381.
- [186] C. Zhang, S. Li, Y. He, C. Chen, S. Jiang, X. Yang, X. Wang, L. Pan, Q. Wan, *IEEE Electron Device Lett.* **2020**, *41*, 617.
- [187] Y. R. Lee, T. Q. Trung, B.-U. Hwang, N.-E. Lee, *Nat. Commun.* **2020**, *11*, 2753.
- [188] H. Tan, Q. Tao, I. Pande, S. Majumdar, F. Liu, Y. Zhou, P. O. Å. Persson, J. Rosen, S. van Dijken, *Nat. Commun.* **2020**, *11*, 1369.
- [189] X. Zhang, Y. Zhuo, Q. Luo, Z. Wu, R. Midya, Z. Wang, W. Song, R. Wang, N. K. Upadhyay, Y. Fang, F. Kiani, M. Rao, Y. Yang, Q. Xia, Q. Liu, M. Liu, J. J. Yang, *Nat. Commun.* **2020**, *11*, 51.
- [190] G. Feng, J. Jiang, Y. Zhao, S. Wang, B. Liu, K. Yin, D. Niu, X. Li, Y. Chen, H. Duan, J. Yang, J. He, Y. Gao, Q. Wan, *Adv. Mater.* **2020**, *32*, 1906171.
- [191] Q. Lu, F. Sun, L. Liu, L. Li, M. Hao, Z. Wang, T. Zhang, *npj Flexible Electron.* **2020**, *4*, 3.
- [192] Y. Kim, Y. J. Kwon, D. E. Kwon, K. J. Yoon, J. H. Yoon, S. Yoo, H. J. Kim, T. H. Park, J.-W. Han, K. M. Kim, C. S. Hwang, *Adv. Mater.* **2018**, *30*, 1704320.
- [193] M. Kumar, H. Kim, J. Kim, *Adv. Mater.* **2019**, *31*, 1900021.
- [194] J. H. Yoon, Z. Wang, K. M. Kim, H. Wu, V. Ravichandran, Q. Xia, C. S. Hwang, J. J. Yang, *Nat. Commun.* **2018**, *9*, 417.
- [195] J. Ge, S. Zhang, Z. Liu, Z. Xie, S. Pan, *Nanoscale* **2019**, *11*, 6591.
- [196] Z. Lv, X. Xing, S. Huang, Y. Wang, Z. Chen, Y. Gong, Y. Zhou, S.-T. Han, *Matter* **2021**, *4*, 1702.
- [197] W. Wang, G. Pedretti, V. Milo, R. Carboni, A. Calderoni, N. Ramaswamy, A. S. Spinelli, D. Ielmini, *Sci. Adv.* **2018**, *4*, eaat4752.
- [198] S. Bolat, G. Torres Sevilla, A. Mancinelli, E. Gilshtein, J. Sastre, A. Cabas Vidani, D. Bachmann, I. Shorubalko, D. Briand, A. N. Tiwari, Y. E. Romanyuk, *Sci. Rep.* **2020**, *10*, 16664.
- [199] M. Giordani, M. Berto, M. Di Lauro, C. A. Bortolotti, M. Zoli, F. Biscarini, *ACS Sens.* **2017**, *2*, 1756.
- [200] N. Liu, Y. Liu, J. Hu, Y. He, X. Zhang, Q. Wan, *Appl. Surf. Sci.* **2019**, *481*, 1412.
- [201] T.-Y. Wang, J.-L. Meng, Z.-Y. He, L. Chen, H. Zhu, Q.-Q. Sun, S.-J. Ding, P. Zhou, D. W. Zhang, *Nanoscale Horiz.* **2019**, *4*, 1293.
- [202] C. J. Wan, Y. H. Liu, L. Q. Zhu, P. Feng, Y. Shi, Q. Wan, *ACS Appl. Mater. Interfaces* **2016**, *8*, 9762.
- [203] N. Liu, L. Q. Zhu, P. Feng, C. J. Wan, Y. H. Liu, Y. Shi, Q. Wan, *Sci. Rep.* **2015**, *5*, 18082.
- [204] Y. Zhao, S. Dai, Y. Chu, X. Wu, J. Huang, *Chem. Commun.* **2018**, *54*, 8186.
- [205] E. Li, W. Lin, Y. Yan, H. Yang, X. Wang, Q. Chen, D. Lv, G. Chen, H. Chen, T. Guo, *ACS Appl. Mater. Interfaces* **2019**, *11*, 46008.
- [206] D. Choi, M.-K. Song, T. Sung, S. Jang, J.-Y. Kwon, *Nano Energy* **2020**, *74*, 104912.
- [207] R. C. Atkinson, R. M. Shiffrin, in *Psychology of Learning and Motivation*, 1st ed. (Ed: B. Ross), Elsevier, Amsterdam **1968**, pp. 89–195.
- [208] T. Ohno, T. Hasegawa, T. Tsuruoka, K. Terabe, J. K. Gimzewski, M. Aono, *Nat. Mater.* **2011**, *10*, 591.
- [209] M.-K. Kim, J.-S. Lee, *ACS Nano* **2018**, *12*, 1680.
- [210] S. Kim, Y. Lee, M. Park, G. Go, Y. Kim, W. Xu, H. Lee, H. Kim, D. Seo, W. Lee, T.-W. Lee, *Adv. Electron. Mater.* **2019**, *5*, 1900008.
- [211] F. Attneave, M. B. , D. O. Hebb, *Am. J. Psychol.* **1950**, *63*, 633.
- [212] O. Bichler, W. Zhao, F. Alibart, S. Pleutin, S. Lenfant, D. Vuillaume, C. Gamrat, *Neural Comput.* **2013**, *25*, 549.

- [213] M. Ziegler, R. Soni, T. Patelczyk, M. Ignatov, T. Bartsch, P. Meuffels, H. Kohlstedt, *Adv. Funct. Mater.* **2012**, *22*, 2744.
- [214] T. Ahmed, S. Kuriakose, E. L. H. Mayes, R. Ramanathan, V. Bansal, M. Bhaskaran, S. Sriram, S. Walia, *Small* **2019**, *15*, 1900966.
- [215] F. Yu, L. Q. Zhu, H. Xiao, W. T. Gao, Y. B. Guo, *Adv. Funct. Mater.* **2018**, *28*, 1804025.
- [216] J. J. Langille, R. E. Brown, *Front. Syst. Neurosci.* **2018**, *12*, 52.
- [217] A. Citri, R. C. Malenka, *Neuropsychopharmacology* **2008**, *33*, 18.
- [218] F. Rosenblatt, *Psychol. Rev.* **1958**, *65*, 386.
- [219] M. Olazaran, *Soc. Stud. Sci.* **1996**, *26*, 611.
- [220] Y. LeCun, Y. Bengio, G. Hinton, *Nature* **2015**, *521*, 436.
- [221] T. P. Lillicrap, A. Santoro, L. Marris, C. J. Akerman, G. Hinton, *Nat. Rev. Neurosci.* **2020**, *21*, 335.
- [222] D. S. Jeong, K. M. Kim, S. Kim, B. J. Choi, C. S. Hwang, *Adv. Electron. Mater.* **2016**, *2*, 1600090.
- [223] S. Dai, Y. Zhao, Y. Wang, J. Zhang, L. Fang, S. Jin, Y. Shao, J. Huang, *Adv. Funct. Mater.* **2019**, *29*, 1903700.
- [224] W. Zhang, B. Gao, J. Tang, P. Yao, S. Yu, M.-F. Chang, H.-J. Yoo, H. Qian, H. Wu, *Nat. Electron.* **2020**, *3*, 371.
- [225] Q. Wan, M. T. Sharbati, J. R. Erickson, Y. Du, F. Xiong, *Adv. Mater. Technol.* **2019**, *4*, 1900037.
- [226] Y. Wu, X. Wang, W. D. Lu, *Semicond. Sci. Technol.* **2022**, *37*, 024003.
- [227] L. R. Iyer, Y. Chua, H. Li, *Front. Neurosci.* **2021**, *15*, 608567.
- [228] Q. Liu, Y. Liu, J. Li, C. Lau, F. Wu, A. Zhang, Z. Li, M. Chen, H. Fu, J. Draper, X. Cao, C. Zhou, *ACS Appl. Mater. Interfaces* **2019**, *11*, 16749.
- [229] J. Li, C. Ge, J. Du, C. Wang, G. Yang, K. Jin, *Adv. Mater.* **2020**, *32*, 1905764.
- [230] M.-K. Kim, J.-S. Lee, *Nano Lett.* **2019**, *19*, 2044.
- [231] Y. van de Burgt, E. Lubberman, E. J. Fuller, S. T. Keene, G. C. Faria, S. Agarwal, M. J. Marinella, A. Alec Talin, A. Salleo, *Nat. Mater.* **2017**, *16*, 414.
- [232] A. Melianas, T. J. Quill, G. LeCroy, Y. Tuchman, H. V. Loo, S. T. Keene, A. Giovannitti, H. R. Lee, I. P. Maria, I. McCulloch, A. Salleo, *Sci. Adv.* **2020**, *6*, eabb2958.
- [233] S. Agarwal, S. J. Plimpton, D. R. Hughart, A. H. Hsia, I. Richter, J. A. Cox, C. D. James, M. J. Marinella, *2016 Int. Joint Conf. on Neural Networks (IJCNN)*, IEEE **2016**, pp. 929–938.
- [234] N. Caporale, Y. Dan, *Annu. Rev. Neurosci.* **2008**, *31*, 25.
- [235] X. Zhang, A. Huang, Q. Hu, Z. Xiao, P. K. Chu, *Phys. Status Solidi* **2018**, *215*, 1700875.
- [236] R. C. Froemke, Y. Dan, *Nature* **2002**, *416*, 433.
- [237] Y. Li, Y. Zhong, J. Zhang, L. Xu, Q. Wang, H. Sun, H. Tong, X. Cheng, X. Miao, *Sci. Rep.* **2015**, *4*, 4906.
- [238] K. A. Buchanan, J. R. Mellor, *Front. Synaptic Neurosci.* **2010**, *2*, 11.
- [239] T. Serrano-Gotarredona, T. Masquelier, T. Prodromakis, G. Indiveri, B. Linares-Barranco, *Front. Neurosci.* **2013**, *7*, 2.
- [240] S. Choi, J. Yang, G. Wang, *Adv. Mater.* **2020**, *32*, 2004659.
- [241] H. Tan, S. Majumdar, Q. Qin, J. Lahtinen, S. van Dijken, *Adv. Intell. Syst.* **2019**, *1*, 1900036.
- [242] S. Majumdar, H. Tan, Q. H. Qin, S. van Dijken, *Adv. Electron. Mater.* **2019**, *5*, 1800795.
- [243] C. Jiang, Y. Zhang, B. Tian, C. Luo, N. Zhong, J. Wang, X. Meng, H. Peng, C.-G. Duan, J. Chu, *J. Mater. Chem. C* **2019**, *7*, 9933.
- [244] L. Zhou, S. Yang, G. Ding, J.-Q. Yang, Y. Ren, S.-R. Zhang, J.-Y. Mao, Y. Yang, Y. Zhou, S.-T. Han, *Nano Energy* **2019**, *58*, 293.
- [245] C. Ma, Z. Luo, W. Huang, L. Zhao, Q. Chen, Y. Lin, X. Liu, Z. Chen, C. Liu, H. Sun, X. Jin, Y. Yin, X. Li, *Nat. Commun.* **2020**, *11*, 1439.
- [246] P. Stoliar, H. Yamada, Y. Toyosaki, A. Sawa, *Sci. Rep.* **2019**, *9*, 17740.
- [247] H. Shim, K. Sim, F. Ershad, P. Yang, A. Thukral, Z. Rao, H.-J. Kim, Y. Liu, X. Wang, G. Gu, L. Gao, X. Wang, Y. Chai, C. Yu, *Sci. Adv.* **2019**, *5*, eaax4961.
- [248] K. He, Y. Liu, M. Wang, G. Chen, Y. Jiang, J. Yu, C. Wan, D. Qi, M. Xiao, W. R. Leow, H. Yang, M. Antonietti, X. Chen, *Adv. Mater.* **2020**, *32*, 1905399.
- [249] M. Karbalaee Akbari, S. Zhuiykov, *Nat. Commun.* **2019**, *10*, 3873.
- [250] H. Wei, R. Shi, L. Sun, H. Yu, J. Gong, C. Liu, Z. Xu, Y. Ni, J. Xu, W. Xu, *Nat. Commun.* **2021**, *12*, 1068.
- [251] S. Zhang, K. Guo, L. Sun, Y. Ni, L. Liu, W. Xu, L. Yang, W. Xu, *Adv. Mater.* **2021**, *33*, 2007350.
- [252] L. Sun, Y. Du, H. Yu, H. Wei, W. Xu, W. Xu, *Research* **2022**, *2022*, 9851843.
- [253] Z. Gao, S. Chen, R. Li, Z. Lou, W. Han, K. Jiang, F. Qu, G. Shen, *Nano Energy* **2021**, *86*, 106078.
- [254] E. R. Kandel, J. D. Koester, S. H. Mack, S. A. Siegelbaum, *Principles of Neural Science*, 6th ed., McGraw Hill, New York **2021**.
- [255] Y. Ugawa, *Neurosci. Res.* **2020**, *156*, 80.
- [256] K. W. Jung, D.-H. Yang, S.-J. Myung, in *Reference Module in Neuroscience and Biobehavioral Psychology*, Elsevier, Amsterdam **2017**, pp. 344–347.
- [257] S. Kim, D. G. Roe, Y. Y. Choi, H. Woo, J. Park, J. I. Lee, Y. Choi, S. B. Jo, M. S. Kang, Y. J. Song, S. Jeong, J. H. Cho, *Sci. Adv.* **2021**, *7*, eabe3996.
- [258] S. I. Head, M. B. Arber, *Adv. Physiol. Educ.* **2013**, *37*, 405.
- [259] S. Jung, H. Lee, S. Myung, H. Kim, S. K. Yoon, S.-W. Kwon, Y. Ju, M. Kim, W. Yi, S. Han, B. Kwon, B. Seo, K. Lee, G.-H. Koh, K. Lee, Y. Song, C. Choi, D. Ham, S. J. Kim, *Nature* **2022**, *601*, 211.
- [260] D. Ielmini, H. S. P. Wong, *Nat. Electron.* **2018**, *1*, 333.
- [261] I. Krauhausen, D. A. Koutsouras, A. Melianas, S. T. Keene, K. Lieberth, H. Ledanseur, R. Sheelamantula, A. Giovannitti, F. Torricelli, I. McCulloch, P. W. M. Blom, A. Salleo, Y. van de Burgt, P. Gkoupidenis, *Sci. Adv.* **2021**, *7*, eabl5068.
- [262] Y. Ni, M. Ma, H. Wei, J. Gong, H. Han, L. Liu, Z. Xu, W. Xu, *Nano Energy* **2021**, *86*, 106038.
- [263] S. Zhang, K. Guo, H. Han, H. Yu, H. Wei, J. Gong, W. Xu, *Adv. Funct. Mater.* **2021**, *31*, 2101917.
- [264] P. Gkoupidenis, D. A. Koutsouras, G. G. Malliaras, *Nat. Commun.* **2017**, *8*, 15448.
- [265] D. A. Koutsouras, G. G. Malliaras, P. Gkoupidenis, *MRS Commun.* **2018**, *8*, 493.
- [266] T. Tuma, A. Pantazi, M. Le Gallo, A. Sebastian, E. Eleftheriou, *Nat. Nanotechnol.* **2016**, *11*, 693.
- [267] T. Tuma, M. Le Gallo, A. Sebastian, E. Eleftheriou, *IEEE Electron Device Lett.* **2016**, *37*, 1238.
- [268] Z.-x. Li, X.-y. Geng, J. Wang, F. Zhuge, *Front. Neurosci.* **2021**, *15*, 717947.
- [269] J.-Q. Yang, R. Wang, Z.-P. Wang, Q.-Y. Ma, J.-Y. Mao, Y. Ren, X. Yang, Y. Zhou, S.-T. Han, *Nano Energy* **2020**, *74*, 104828.
- [270] Y. Li, J. Lu, D. Shang, Q. Liu, S. Wu, Z. Wu, X. Zhang, J. Yang, Z. Wang, H. Lv, M. Liu, *Adv. Mater.* **2020**, *32*, 2003018.
- [271] P. C. Harikesh, C. Yang, D. Tu, J. Y. Gerasimov, A. M. Dar, A. Armada-Moreira, M. Massetti, R. Kroon, D. Bliman, R. Olsson, E. Stavrinidou, M. Berggren, S. Fabiano, *Nat. Commun.* **2022**, *13*, 901.



**Yeongjun Lee** is a postdoctoral researcher in the Department of Chemical Engineering at Stanford University, USA. He received his B.S. in the Department of Materials Science and Engineering (MSE) from Hanyang University, South Korea in 2012. He received his Ph.D. in the MSE from Pohang University of Science and Technology (POSTECH), South Korea in 2018. He joined the MSE at Seoul National University, as a postdoctoral researcher and worked at Organic Material Lab in Samsung Advanced Institute of Technology as a staff researcher (2019–2021). His research interests include stretchable electronics and neuromorphic devices that use printed organic nanomaterials.



**Jin Young Oh** is an assistant professor in the Department of Chemical Engineering at Kyung Hee University. He earned his Ph.D. in Materials Science and Engineering from Yonsei University in 2014 and was a postdoctoral fellow at Stanford University from 2015 to 2018. His current research focuses on developing skin-inspired electronics for applications in smart health care.



**Tae-Woo Lee** is a professor in the Department of MSE at Seoul National University, South Korea. He received his Ph.D. in Chemical Engineering from KAIST, South Korea in 2002. He joined Bell Laboratories, USA, as a postdoctoral researcher and worked at Samsung Advanced Institute of Technology as a research staff (2003–2008). He was an associate professor in MSE at Pohang University of Science and Technology (POSTECH), South Korea, until August 2016. His research focuses on printed or soft electronics that use organic and organic-inorganic hybrid materials for flexible/stretchable displays, solid-state lighting, solar energy conversion devices, and bioinspired neuromorphic devices.